Structural and mechanistic insights into human choline and ethanolamine transport

Keiken Ri[1-5†], Tsai-Hsuan Weng[6†], Ainara Claveras Cabezudo[7,8†], Wiebke Jösting[6], Zhang Yu[1], Andre Bazzone[9], Nancy C.P. Leong[1-5], Sonja Welsch[10], Raymond T. Doty[11], Gonca Gursu[6], Tiffany Jia Ying Lim[1-5], Sarah Luise Schmidt[6], Janis L. Abkowitz[11], Gerhard Hummer[7,12*], Di Wu[6,15*], Long N Nguyen[1-5*], Schara Safarian[6,13-15*]

Affiliations

[1] *Department of Biochemistry, Yong Loo Lin School of Medicine, National University of Singapore, Singapore 119228*

[2] *Immunology Program, Life Sciences Institute, National University of Singapore, Singapore 117456*

[3] *Singapore Lipidomics Incubator (SLING), Life Sciences Institute, National University of Singapore, Singapore 117456*

[4] *Cardiovascular Disease Research (CVD) Programme, Yong Loo Lin School of Medicine, National University of Singapore, Singapore 117545*

[5] *Immunology Translational Research Program, Yong Loo Lin School of Medicine, National University of Singapore, Singapore 117456*

[6] *Department of Molecular Membrane Biology, Max Planck Institute of Biophysics, D-60438 Frankfurt/Main, Germany*

[7] *Department of Theoretical Biophysics, Max Planck Institute of Biophysics, D-60438 Frankfurt/Main, Germany*

[8] *IMPRS on Cellular Biophysics, D-60438 Frankfurt/Main, Germany*

[9] *Nanion Technologies GmbH, Ganghoferstr. 70a, 80339, Munich, Germany*

[10] *Central Electron Microscopy Facility, Max Planck Institute of Biophysics, D-60438 Frankfurt am Main, Germany*

[11] *Division of Hematology, Department of Medicine, University of Washington, Seattle, WA, 98195, USA*

[12] *Institute of Biophysics, Goethe University Frankfurt, D-60438 Frankfurt/Main, Germany*

[13] *Institute of Clinical Pharmacology, Goethe University Frankfurt, D-60438 Frankfurt/Main, Germany*

[14] *Fraunhofer Cluster of Excellence for Immune Mediated Diseases CIMD, D-60438 Frankfurt/Main, Germany*

[15] *Fraunhofer Institute for Translational Medicine and Pharmacology ITMP Frankfurt, D-60438 Frankfurt/Main, Germany*

[*]Correspondence and requests for materials should be addressed to Gerhard Hummer (gerhard.hummer@biophys.mpg.de), Di Wu (di.wu@biophys.mpg.de), Long Nguyen (bchnnl@nus.edu.sg), and Schara Safarian (schara.safarian@biophys.mpg.de).

[†]These authors contributed equally.

Abstract

Human feline leukemia virus subgroup C receptor-related proteins 1 and 2 (FLVCR1 and 2) are members of the major facilitator superfamily[1]. Their dysfunction is linked to several clinical disorders, including PCARP, HSAN, and Fowler syndrome[2–7]. Earlier studies concluded that FLVCR1 may function as a putative heme exporter[8–12], while FLVCR2 was suggested to act as a heme importer[13], yet conclusive biochemical and detailed molecular evidence remained elusive for the function of both transporters[14–17]. Here, we show that FLVCR1 and FLVCR2 facilitate the transport of choline and ethanolamine across human plasma membranes, utilizing a concentration-driven substrate translocation process. Through structural and computational analyses, we have identified distinct conformational states of FLVCRs and unraveled the coordination chemistry underlying their substrate interactions. Within the binding pocket of both transporters, we identify fully conserved tryptophan and tyrosine residues holding a central role in the formation of cation-π interactions, essential for choline and ethanolamine selectivity. Our findings not only clarify the mechanisms of choline and ethanolamine transport by FLVCR1 and FLVCR2, enhancing our comprehension of disease-associated mutations that interfere with these vital processes, but also shed light on the conformational dynamics of these MFS-type proteins during the transport cycle.

59 **Introduction**

60 The feline leukaemia virus subgroup C receptor (FLVCR) family, a member of the major
61 facilitator superfamily (MFS) of secondary active transporters, consists of four paralogues encoded by
62 the human *SLC49* gene group[1]. FLVCR1 (SLC49A1) was initially identified as the cell surface receptor
63 for feline leukaemia virus (FeLV)[18]. FLVCR2 (SLC49A2) shares 60% sequence identity with FLVCR1 in the
64 transmembrane domain but does not bind the feline leukaemia virus subgroup C envelope protein[19].
65 Both transporters exhibit ubiquitous tissue distribution in humans and have significant haemato- and
66 neuropathological implications[1,17]. Dysfunction of FLVCR1 caused by germline mutations is associated
67 with posterior column ataxia with retinitis pigmentosa (PCARP)[2,3], and hereditary sensory and
68 autonomic neuropathies (HSANs)[4,5]. Similarly, truncation and missense mutations in *FLVCR2* are
69 associated with autosomal-recessive cerebral proliferative vasculopathy (Fowler syndrome)[6,7].
70 Furthermore, both FLVCR variants are suggested to play a key role in cell development and
71 differentiation, including angiogenesis and tumorigenesis[20–23].

72

73 Earlier studies concluded that FLVCR1 may function as a putative heme exporter[8–12], while
74 FLVCR2 was suggested to act as a heme importer[13], yet their definitive roles in this capacity remain
75 elusive[14–17]. To accurately understand their functions, experimental validation at the biochemical and
76 molecular levels is necessary, which will connect these transporters' physiological roles and clinical
77 relevance to their specific mechanistic actions. Recent studies indicated FLVCR1 is involved in choline
78 transport, however, the ligands for FLVCR2 still remain elusive[24]. Here, we used an integrative
79 approach, including cell-based radioligand transport assays, single-particle analysis (SPA) cryogenic-
80 electron microscopy (cryo-EM), structure-guided mutagenesis, and atomistic molecular dynamics (MD)
81 simulations to characterize the ligand specificity, molecular architecture, and the conformational
82 landscape of FLVCR1 and FLVCR2 transporters.

83 **Results**

84 ***Choline and ethanolamine are transport substates of* FLVCR1 and FLVCR2**

85 We expressed the human *FLVCR1* and *FLVCR2* genes in human embryonic kidney (HEK293)
86 cells to substantiate and characterize their roles in cellular choline and ethanolamine transport[25,26].
87 Upon overproduction, FLVCR1a (hereafter referred to as FLVCR1) and FLVCR2 localized at the plasma
88 membrane of HEK293 cells (Fig. 1a and Supplementary Fig. 1a-d). Radioactive [^{3}H] choline transport
89 assays showed a discernible increase in uptake facilitated by the FLVCR2, whereas FLVCR1 did not
90 exhibit such an effect under the tested condition (Extended Data Fig. 1a). Notably, co-expression of
91 the choline kinase A (*CHKA*) gene significantly enhanced choline uptake by both transporters in dose-
92 and time-dependent manners (Fig. 1b-d). This suggests that choline influx mediated by FLVCR1 and
93 FLVCR2 is enhanced by the overproduction of downstream choline-utilizing enzymes. In order to
94 ascertain whether choline is the principal physiological substrate for FLVCR1, a comprehensive
95 metabolomic analysis was performed on liver samples from FLVCR1 knockout mice (Extended Data Fig.
96 2a). This led us to discover that, in addition to choline and its metabolites, ethanolamine metabolite
97 profiles were also affected in FLVCR1 knockout livers (Extended Data Fig. 2b,c). Subsequent cell-based
98 assays revealed that both FLVCRs facilitate ethanolamine uptake into cells (Extended Data Fig. 1b).
99 Notably, co-expression of *ETNK-1* enhanced the ethanolamine transport rate of FLVCR1 by five-fold,
100 but did not substantially affect the efficiency of FLVCR2 (Fig. 1e-g and Extended Data Fig. 1b). We
101 determined transport kinetic parameters of FLVCR1 and FLVCR2, revealing K_m values of 47.4 ± 9.8 μM
102 and 64.0 ± 21.0 μM for choline, 8 ± 1.5 μM and 41.5 ± 32.0 μM for ethanolamine, respectively (Fig.
103 1c,f). To decipher the transport mechanism of both FLVCRs, we investigated their reliance on sodium
104 ions and pH levels. Our uptake studies revealed that FLVCR-mediated transport of choline and
105 ethanolamine is not contingent upon sodium ion involvement and operates effectively across a broad
106 pH range (Extended Data Fig. 3a,b). This finding underscores that neither sodium nor pH gradients are
107 critical for the translocation of choline and ethanolamine by FLVCRs. Next, we further assessed the
108 mechanistic properties of FLVCR2 by performing a choline washout assay. Upon inverting the choline
109 gradient across the plasma membrane, we measured a significant decrease of cellular choline levels

110 within 1 h indicating for a bidirectional choline transport activity mediated by FLVCR2 (Extended Data
111 Fig. 3c). FLVCR1 showed similar properties in an ethanolamine washout experiment (Extended Data
112 Fig. 3c). Our findings suggest that both FLVCR1 and FLVCR2 operate as uniporters, facilitating downhill
113 ligand transport independent of sodium or pH gradients but aided by the typically negative membrane
114 potential[27].
115
116 ***FLVCR architecture and conformational landscape***
117 Next, we aimed to establish structure-function relationships for the choline and ethanolamine
118 transport properties of FLVCR1 and FLVCR2. Wildtype FLVCR1 and FLVCR2 proteins were purified and
119 subjected to SPA cryo-EM (Supplementary Fig. 1a-f). We determined inward-facing conformation
120 structures of FLVCR1 and FLVCR2 in their apo states at 2.9 Å resolution (Fig. 2a,b, and Supplementary
121 Fig. 2,3). In addition, we successfully elucidated the outward-facing conformational structure of
122 FLVCR2 at 3.1 Å resolution from the same sample preparation (Fig. 2c and Supplementary Fig. 3). Both
123 FLVCR paralogs share a common MFS-type architecture[28], with their N-domain containing
124 transmembrane domain (TMs) 1-6 and the C-domain containing TMs 7-12 connected by a long and
125 flexible loop containing two short horizontal cytoplasmic helices (H1 and H2) (Extended Data Fig. 4a,b).
126 In the FLVCR2 structure, we resolved a short helical segment at the C-terminus (H3), while the density
127 of the FLVCR1 C-terminus was less pronounced (Extended Data Fig. 4a,b and Supplementary Fig. 4).
128 Further, we identified an N-linked glycosylation site at N265 of FLVCR1 which locates within the
129 extracellular loop connecting TMs 5 and 6 (EL5-6) (Fig. 2a). In contrast, no glycosylation site was
130 identified in the FLVCR2 structure[19] (Fig. 2b,c and Supplementary Fig. 5).
131 The inward-facing conformations of FLVCR1 and FLVCR2 exhibit a close resemblance to each
132 other, with a root mean square deviation (Cα r.m.s.d.) of 0.993 Å (Extended Data Fig. 4b). Both
133 structures feature a wedge-shaped solvent-accessible cavity that is mainly created by the separation
134 of TMs 4 and 5 of the N-domain from TMs 10 and 11 of the C-domain (Fig. 2d and Extended Data Fig.
135 4b and 5a). This space extends halfway across the membrane with a similar depth of around 23 Å in
136 both transporters. On the level of the outer leaflet, TMs 1, 2, and 5 of the N-domain and TMs 7, 8, and

137 11 of the C-domain pack tightly against each other and thus shield the central cavity from the
138 extracellular space (Fig. 2d and Extended Data Fig. 4b and 5a). Notably, TMs 1, 4, and 7 exhibit
139 disordered regions at their C-terminal ends, followed by short kinked helical motifs designated TMs 1b,
140 4b, and 7b (Fig. 2d and Extended Data Fig. 4a and 5a).

141 The outward-facing conformation of FLVCR2 features a cavity accessible from the extracellular
142 space. This cavity is formed through a 'rocker-switch' rigid-body motion that occurs during the
143 transition from the inward- to outward-facing state (Fig. 2d, e and Supplementary Video 1). This
144 motion involves a shift of the outer halves of all transmembrane segments away from the central axis.
145 Concurrently, the inner halves of these TMs move inward, effectively blocking the exit pathway. (Fig.
146 2e). The cavities in outward- and inward-facing conformations are 7.4 Å and 8.6 Å wide at their
147 respective openings (Fig. 2d). Both inward- and outward-facing cavities are lined by uncharged and
148 hydrophobic residues which are mostly conserved (Extended Data Fig. 6). Compared to the inward-
149 facing cavity, the outward-facing cavity demonstrates a more restricted pathway within its central
150 region. In this narrowed segment of the cavity, the channel ends at $W102^{FLVCR2}$ and $Y325^{FLVCR2}$
151 (equivalent to $W125^{FLVCR1}$ and $Y349^{FLVCR1}$), two residues that are highly conserved in both FLVCR
152 transporters (Fig. 2d and Extended Data Fig. 5a and 6).

153 In line with an alternating-access model, the inward-facing conformation of FLVCR2 features a
154 tightly-sealed extracellular gate created by inter-domain interactions. This is mainly achieved by the
155 juxtaposition of TM1b (N-domain) and TM7b (C-domain) (Fig. 2d and Extended Data Fig. 4b). The inter-
156 domain interaction between these two motifs is stabilized by a hydrogen bonding network consisting
157 of two pseudo-symmetry-related asparagine residues $N110^{FLVCR2}$ and $N332^{FLVCR2}$, and $E343^{FLVCR2}$ (TM8)
158 and $N239^{FLVCR2}$ (EL5-6) (Extended Data Fig. 5a and Supplementary Fig. 6a). Furthermore, we identified
159 a stable inter-domain salt bridge between $D124^{FLVCR2}$ (TM2) and $R333^{FLVCR2}$ (TM7b), reinforcing the
160 external occlusion (Extended Data Fig. 5a and Supplementary Fig. 6b). Our cell-based mutagenesis
161 studies show that alanine substitutions at $N110^{FLVCR2}$, $E343^{FLVCR2}$, $D124A^{FLVCR2}$ and $R333A^{FLVCR2}$
162 individually result in a significant decrease of choline uptake and an almost complete perturbation of
163 ethanolamine transport, highlighting a critical role of inter-domain interactions on the extracellular

164 surface for FLVCR2 functionality (Extended Data Fig. 5b and Supplementary Fig. 7). While FLVCR1
165 exhibits a similar extracellular hydrogen bonding network as FLVCR2, it lacks a corresponding salt
166 bridge interaction (Extended Data Fig. 5a). Notably, the disruption of the hydrogen bond between
167 N133^{FLVCR1} and N359^{FLVCR1} (structurally analogous to N110^{FLVCR2} and N332^{FLVCR2}) through an alanine
168 substitution of N133^{FLVCR1} markedly diminishes FLVCR1's transport activity for both choline and
169 ethanolamine. In contrast, the E367A^{FLVCR1} mutation impacts the transport of choline to a stronger
170 extend as compare to ethanolamine transport (Extended Data Fig. 5c).

171 During the transition from inward- to outward-facing conformation of FLVCR2, inter-domain
172 interactions contributing to the extracellular gate become disrupted, while the formation of the
173 intracellular gate occludes the central cavity from the cytoplasmic side. TM4b of the N-domain moves
174 in proximity to the N-terminal end of TM11 of the C-domain to establish a first level of occlusion (Fig.
175 2d,e). An interaction network consisting of several hydrogen bonds and a salt bridge is found within
176 this region as well (Extended Data Fig. 5a). The E435^{FLVCR2} residue in TM11 plays a pivotal and
177 multifaceted role, forming a hydrogen bond with S203^{FLVCR2} and simultaneously establishing a salt
178 bridge with R200^{FLVCR2} in TM4b (Extended Data Fig. 5a and Supplementary Fig. 6b). Individuals with a
179 homozygous S203Y mutation in FLVCR2 are nonviable, likely attributable to the complete loss of
180 choline and ethanolamine transport activity[29] (Fig. 1b,c). Our mutagenesis studies underscore a greater
181 significance of S203^{FLVCR2} compared to R200^{FLVCR2}, particularly in choline transport (Fig. 1b and Extended
182 Data Fig. 5b). This suggests that the interaction between E435^{FLVCR2} and S203^{FLVCR2} is essential for either
183 facilitating conformational changes during the transport cycle or maintaining the stability of FLVCR2 in
184 its outward-facing state. An additional inter-domain hydrogen bond is identified between S199^{FLVCR2} in
185 TM4b and S439^{FLVCR2} in TM1 (Extended Data Fig. 5a and Supplementary Fig. 6a). In the peripheral region,
186 K372^{FLVCR2} and R374^{FLVCR2} (EL8-9) approach N209^{FLVCR2} (EL4-5) and S212^{FLVCR2} (TM5) to form hydrogen
187 bond pairs and thus block the lateral accessibility of the cavity (Extended Data Fig. 5a and
188 Supplementary Fig. 6a). A second level of occlusion was observed beneath the cytoplasmic ends of
189 TMs 4, 10 and 11, where H1 and H3 are positioned in close proximity (Extended Data Fig. 5a). Here,
190 the backbone carbonyl group and amide nitrogen of A283^{FLVCR2} (H1) form stable hydrogen bonds with

191 N497^{FLVCR2} (H3) and Y431^{FLVCR2} (IL10-11), respectively (Extended Data Fig. 5a and Supplementary Fig.
192 6a). Together with the loop connecting TMs 10 and 11, the two helical motifs H1 and H3 serve as a
193 cytoplasmic latch to secure the closure of the two domains.
194
195 ***Choline binding and coordination chemistry of FLVCR1 and FLVCR2***
196 To decipher the substrate binding and coordination chemistry of FLVCR1 and FLVCR2, we
197 employed choline as a ligand and determined their structures at resolutions of 2.6 Å and 2.8 Å,
198 respectively (Fig. 3a,b and Supplementary Fig. 2, 3 and 4d,e). Both structures were captured in the
199 inward-facing conformation, suggesting that choline is capable of resolving the previously captured
200 conformational heterogeneity of FLVCR2. The choline-bound structures exhibit a Cα r.m.s.d. of 0.688
201 Å (FLVCR1) and 1.002 Å (FLVCR2), respectively, compared to their apo inward-facing structures
202 (Extended Data Fig. 7a,b). In the choline-bound structures, the binding sites are located at analogous
203 positions, with the choline molecule situated between the two domains, surrounded mainly by TMs 1,
204 2, 4, 5, 7, and 11 (Fig. 3a,b). The binding site in both transporters comprises an identical composition
205 of conserved residues. We observed that W102^{FLVCR1} and W125^{FLVCR2} in TM1 directly interact with
206 choline. This central coordinating tryptophan residue is located above choline, protruding its side chain
207 to constrain the diffusion of the molecule towards the extracellular space (Fig. 2d and Fig 3c,d). Two
208 additional aromatic residues of TM7, one tyrosine (Y325^{FLVCR1} and Y349^{FLVCR2}) and one phenylalanine
209 (F348^{FLVCR1} and F324^{FLVCR2}), line the peripheral space of the binding site and restrict the movement of
210 choline within the pocket. Our MD simulations demonstrate that the quaternary ammonium group of
211 choline forms stable cation-π interactions with the conserved tryptophan (W125^{FLVCR1} and W102^{FLVCR2})
212 and tyrosine residues (Y325^{FLVCR1} and Y349^{FLVCR2}) in a simultaneous manner (Fig. 3c,d). Mutations of
213 W125A^{FLVCR1} and W102A^{FLVCR2} significantly reduced choline transport activity (Fig. 3e and
214 Supplementary Fig. 7). MD simulations further confirmed the key role of the tryptophan in both
215 transporters (Fig. 3f,g). We also found that the hydroxyl group of choline is essential for ligand
216 recognition by both FLVCRs. Substitution to a carboxylic group as found in betaine abolishes ligand
217 binding and transport activity[26] (Fig. 3h). In our choline simulations, this hydroxyl shows versatile

218 interactions by forming transient hydrogen bonds with two proximal asparagine residues
219 (Q214^{FLVCR1}/Q471^{FLVCR1}, Q191^{FLVCR2}/Q447^{FLVCR2}). Further interactions come from at least two water
220 molecules that were consistently present around the hydroxyl moiety of the choline (Supplementary
221 Fig. 8 and Supplementary Video 2). Functional analyses of Q214^{FLVCR1}, Q471^{FLVCR1}, Q191^{FLVCR2}, and
222 Q447^{FLVCR2} indicate that changes of the local protein environment around the hydroxyl group of choline,
223 caused by alanine substitutions, discernibly affect the transport activities of both FLVCRs (Fig. 3e). It is
224 noteworthy that all these residues are fully conserved in mammalian FLVCR homologs, suggesting a
225 common substrate profile of FLVCRs across species (Fig. 3i).
226
227 ***Molecular mechanism of ligand selectivity of FLVCR1***
228 Guided by our functional analyses, we advanced our investigation into the molecular
229 mechanism of ethanolamine binding by FLVCR1. We obtained the cryo-EM structure of FLVCR1
230 complexed with ethanolamine at a resolution of 3.1 Å, showing an inward-facing conformation
231 analogous to the choline-bound FLVCR1 structure (Fig. 4a, Extended Data Fig. 7c and Supplementary
232 Fig. 2). The ethanolamine density was identified within the abovementioned ligand binding-pocket,
233 with its primary amine group engaging in cation-π interactions with the conserved W125^{FLVCR1} and
234 Y349^{FLVCR1} residues (Fig. 4b, and Supplementary Fig. 4f). Our cryo-EM data, corroborated by MD
235 simulations, indicate that ethanolamine is positioned slightly further from W125^{FLVCR1} and Y349^{FLVCR1}
236 than choline, attributable to differences in their molecular orientations (Fig. 3a, 4a and 4c, and
237 Extended Data Fig. 8). While the quaternary ammonium group of choline is situated near Q214^{FLVCR1},
238 ethanolamine's orientation results in its amine group being distanced, consequently bringing its
239 hydroxyl group into closer proximity to Q214^{FLVCR1} (Fig. 4d). These nuanced molecular differences
240 presumably contribute to the selective substrate profile of FLVCR1 as observed in our cell-based
241 transport assays where FLVCR1 showed a preferential ethanolamine transport activity (Fig. 1b, c, 3e
242 and 4e). This is further substantiated by the Q214A^{FLVCR1} mutant variant, which results in a complete
243 loss of ethanolamine transport activity while only partially affecting choline transport (Fig. 3e and 4e).

244 Notably, alanine substitution of the analogous Q191^{FLVCR2} residue abolishes the transport of both
245 ethanolamine and choline in FLVCR2 (Fig. 3e and 4e).
246
247 ***Identification of a peripheral heme binding site of FLVCR2***
248 Our cell-based assays, using hemin as a heme analog substrate, revealed that unlike the
249 choline and ethanolamine uptake data, neither FLVCR1 nor FLVCR2 demonstrated heme import
250 activity (Fig. 5a). This observation was confirmed by our structural studies which did not reveal any
251 density for bound heme molecules within the ligand binding cavities of FLVCR1 or FLVCR2, respectively
252 (Fig. 5b). Of note, neither the dimensions, nor the residues lining the central cavities of both FLVCRs
253 indicate a structural adaptation for accommodating a heme molecule as observed in other heme
254 transporters[30–32].
255 However, upon determining the structure of FLVCR2 in the presence of heme we noticed that
256 heme resolved the previously characterized conformational heterogeneity, fully driving the
257 transporter into the outward-facing conformation (Fig. 5b and Supplementary Fig. 9). Additionally, we
258 identified a density near the N-terminus of TM1 on the intracellular side of FLVCR2, likely
259 corresponding to heme. This density appears to have replaced a peripherally bound lipid molecule that
260 we had previously observed in the outward-facing density map of apo FLVCR2 (Fig. 5b). The protein
261 surface in this particular region displays a patch of positive charges, suggesting the heme molecule to
262 be held in place by the formation of electrostatic interactions between its two propionate groups and
263 the side chains of R81^{FLVCR2}, R82^{FLVCR2}, and K273^{FLVCR2} (Fig. 5b and Extended Data Fig. 6). The map density
264 of bound heme in our structure indicates local mobility of the heme, possibly due to the absence of
265 axial coordination of the central iron in the macrocycle scaffold (Fig. 5b). By contrast, cryo-EM studies
266 on FLVCR1 in the presence of heme did not reveal any heme binding or notable conformational
267 changes.
268 To further investigate heme binding in FLVCR2, MD simulations were performed within a lipid
269 bilayer. Heme was found to interact with the intracellular loop region rather than accessing the central
270 cavity, in agreement with prior functional and structural observations (Supplementary Video 3). When

271 placed near the binding site at the N-terminus of TM1 as indicated by our cryo-EM data, heme rapidly
272 disengaged from R82^{FLVCR2}, yet maintained contact with R83^{FLVCR2}, K273^{FLVCR2}, and I270^{FLVCR2} after
273 insertion into the lipid bilayer (Fig. 5c,d and Supplementary Fig. 10). Subsequent simulations with
274 alanine substitution variants of these residues led to either reduction or complete loss of heme-binding
275 events, indicating the involvement of these residues for FLVCR2 interaction with heme (Fig. 5e).
276 Follow-up structural studies conducted in a competitive manner by the presence of both heme
277 and choline revealed that choline binding occurs within the central cavity of FLVCR2 irrespective of the
278 presence of heme and triggers conformational shifts towards the inward-facing state. This occurs
279 despite heme's ability to drive FLVCR2 into an outward-facing conformation in the absence of choline
280 (Fig. 5f and Supplementary Fig. 9). Our results from the cell-based transport assays showed that the
281 introduction of mutations at the heme-binding residues marginally influenced the choline and
282 ethanolamine transport function of FLVCR2 (Fig. 5g). Nevertheless, co-incubation of heme with either
283 choline or ethanolamine did not impact the transport activity of these ligands in FLVCR2 (Fig. 5h). In
284 conclusion, our structural studies reveal a peripheral heme binding site in FLVCR2 that does not play a
285 critical role in choline and ethanolamine transport.
286
287 ***Translocation pathway of choline and ethanolamine in FLVCRs***
288 MFS transporters typically cycle between inward- and outward-facing conformations,
289 facilitating substrate translocation in an alternating-access manner, and substrate binding plays a
290 pivotal role in eliciting the conformational transitions[33]. Our cryo-EM data supports this mechanism in
291 FLVCR2, where we see a full transition from the outward-facing to inward-facing state upon choline
292 binding. Complementary to our structural insights into the conformational landscape, we performed
293 MD simulations to map the route for choline entry along the pathway in the outward-facing
294 conformation of FLVCR2. After spontaneously diffusing into the translocation pathway, choline initially
295 interacts with several residues near the protein surface, mainly D124^{FLVCR2} (Supplementary Fig. 11). It
296 sequentially approaches the deeper recesses of the cavity, primarily engaging with conserved aromatic
297 residues W102^{FLVCR2} and Y325^{FLVCR2}. In one of the entry events, we observed choline moving

298 spontaneously to a position below the W102^{FLVCR2} residue within the binding site consistent with our
299 structural data (Supplementary Video 4).

300 The substantial global conformational changes triggered by substrate further alter the local
301 arrangement of substrate-coordinating residues within the translocation pathway as seen in our cryo-
302 EM maps. The rearrangement of the binding site results in a more constricted pocket, promoted by
303 the inward movement of the conserved residues towards the substrate molecule (Extended Data Fig.
304 9a). The repositioning of these residues, especially the conserved aromatic side chains W102^{FLVCR2},
305 F324^{FLVCR2}, and Y325^{FLVCR2}, (equivalent to W125^{FLVCR1}, F348F^{LVCR1}, and Y349^{FLVCR1}) restricts the
306 accessibility of the binding pocket and promotes substrate engulfment and coordination. In their
307 choline-bound structures, the cavities of both FLVCRs share common characteristics, exhibiting a
308 neutral interior but a negatively charged surface at the exit (Extended Data Fig. 6b, e). FLVCR1 features
309 a slightly smaller cavity volume of 513 Å^3 compared to 579 Å^3 of FLVCR2 (Extended Data Fig. 9b). While
310 the cavity narrows toward the intracellular side, a peripheral solvent-accessible channel emerging
311 from the cytoplasmic space to the binding site reveals a semi-open translocation pathway in the
312 substrate-bound inward-facing conformations of both transporters, which may facilitate the release
313 of the bound ligand (Extended Data Fig. 9b).

314

315 **Discussion**

316 While FLVCR1 has many studies linking its activity to heme export[8–12], the study of FLVCR2-
317 mediated heme uptake has not been confirmed[13], and furthermore, conclusive biochemical and
318 detailed molecular evidence had remained elusive for the function of both transporters[14–17]. In this
319 study, we have investigated the choline and ethanolamine transport properties of FLVCR1 and FLVCR2
320 via cell-based transport assays and determined cryo-EM structures of human FLVCR variants in distinct
321 apo, choline-bound, and ethanolamine-bound states. Our work provides valuable insights into
322 architecture, ligand binding-chemistries, and conformational landscapes of these two MFS
323 transporters. Via multiple lines of evidence, we arrive at the conclusion that choline and ethanolamine
324 represent primary transport substrates of both FLVCR1 and FLVCR2, while also revealing a peripheral
325 heme-binding site of FLVCR2 with yet unknown functional implications[10,16]. Our findings suggest that
326 both FLVCR1 and FLVCR2 operate as uniporters, facilitating downhill ligand transport independent of
327 sodium or pH gradients. Notably, FLVCR1 and FLVCR2 possess similar ligand binding and coordination
328 chemistries in which a key conserved tryptophan residue ($W125A^{FLVCR1}$ /$W102A^{FLVCR2}$) forms a cation-π
329 interaction with the ammonium and amine groups of the respective ligands. Further, we characterized
330 the functional importance of several glutamine residues within the substrate-binding site that
331 participate in hydrogen bonds with the hydroxyl groups of choline and ethanolamine during ligand
332 coordination or transport. Functional assays point to a ligand preference between FLVCR1 and FLVCR2.
333 Our structural studies suggest that ligand coordination is a crucial determinant of the transport
334 preference between choline and ethanolamine for both FLVCRs. Given that most solute carrier
335 transporters exhibit ligand promiscuity[34,35], the specific role of FLVCR1 as an ethanolamine transporter
336 and FLVCR2 as a choline transporter in physiological conditions has yet to be confirmed through *in vivo*
337 studies in animal models.

338 Based on our structural findings and simulation data, we suggest a rocker-switch alternating-
339 access mechanism for the transport cycle of choline import (Fig. 6, and Supplementary Video 4 and 5).
340 We propose a transport cycle model for both FLVCRs in which the outward-facing conformation
341 represents the state for ligand binding from the extracellular space. Substrate-induced conformational

342 changes drive the transporter towards its inward-facing state. Finally, ligands are released to the
343 intracellular space to enter metabolic pathways. Subsequent to choline-release, FLVCRs will undergo
344 additional conformation changes to adopt their outward-facing state in order to re-initiate the
345 transport cycle. Our structural data did not reveal fully occluded conformations that are key features
346 of alternating access. Hence, we suspect that these occluded conformations exist only transiently and
347 rapidly convert towards either the inward- or outward-facing conformations[33,36,37].

348 In summary, our research delineates the structural framework through which FLVCR1 and
349 FLVCR2 mediate the cellular transport of choline and ethanolamine. Identifying these proteins as
350 facilitative transporters provides a crucial groundwork for future characterizations of the physiological
351 functions of choline and ethanolamine transport *in vivo*. Furthermore, our findings provide
352 mechanistic insights for understanding of the disease-mechanisms pertaining to the mutations of
353 these essential genes.

354

355 **Online Methods**

356 **Generation of inducible HEK293 stable cell lines**

357 The complementary DNAs of full-length wildtype FLVCR1 (human SLC49A1, NCBI Reference Sequence
358 NM_014053) and FLVCR2 (human SLC49A2, NCBI Reference Sequence: NM_017791) were cloned into
359 pcDNA5/FRT/TO (Invitrogen) vectors, respectively. The gene for both FLVCRs was modified by a C-
360 terminal FLAG fusion tag. Further details are found in sequence data provided as supplementary
361 information (Supplementary Tables 2 and 3). The recombinant Flp-In T-REx293-FLVCR1 and Flp-In T-
362 REx293-FLVCR2 cell lines were generated by using a tetracycline-inducible and commercially available
363 Flp-In T-REx host-cell line system from Invitrogen. Flp-In T-REx293 cells were cultured in high-glucose
364 Dulbecco's Modified Eagle's Medium (DMEM; Sigma-Aldrich) supplemented with 10% fetal bovine
365 serum (FBS; Gibco), 1% Pen/Strep (Gibco), 1 µg ml^{-1} Zeocin (Thermo Fisher), and 15 µg ml^{-1} blasticidin
366 S hydrochloride (AppliChem) at 37 °C in an atmosphere of 5% CO_2. Cells were not tested for
367 mycoplasma contamination. For stable integration, the pcDNA5/FRT-FLVCR1-FLAG and pcDNA5/FRT-
368 FLVCR2-FLAG vectors were cotransfected with the Flp recombinase encoding expression vector pOG44
369 (Thermo Fisher) at a 1:13 mass ratio, respectively. All transfection procedures were performed with
370 Lipofectamine™ 2000 reagent according to the manufacturer's instructions (Thermo Fisher). To select
371 for stable clones, transfected cells were cultivated with growth medium containing 100 µg ml^{-1}
372 hygromycin B (AppliChem).

373 **Transport assays in HEK293 cells**

374 HEK293 cells were co-transfected with pcDNA3.1 plasmid and human *FLVCR1* or *FLVCR2* and human
375 choline kinase A (*CHKA*) for choline transport assays or ethanolamine kinase 1 (*ETNK-1*) for
376 ethanolamine transport assays using Lipofectamine™ 2000 reagent (Thermo Fisher Scientific). After 24
377 hours post-transfection, cells were incubated with DMEM containing 20 µM [^{3}H] choline or 2.5 µM [^{14}C]
378 ethanolamine. The cells were incubated at 37 °C and 5% CO_2 for 1 hour for uptake of the ligands. The
379 cells were subsequently washed with ice-cold plain DMEM and lysed with RIPA buffer by shaking for
380 30 minutes. The cell lysates were also quantified by scintillation counter Tricarb. Radioactive signals
381 from cell lysates were normalized to total protein levels. For dose curve assays, indicated

382 concentrations of choline and ethanolamine were incubated with the cells for 1 hour at 37 °C. For time
383 course assays, the cells were incubated with 20 μM [^{3}H] choline or with 2.5 μM [^{14}C] ethanolamine.
384 The transport assays were stopped at indicated time points by adding ice-cold plain DMEM. For testing
385 transport activity of FLVCR1 mutants, 20 μM [^{3}H] choline and 2.5 μM [^{14}C] ethanolamine was used. For
386 testing transport activity of FLVCR2 mutants, 100 μM [^{3}H] choline and 2.5 μM [^{14}C] ethanolamine was
387 used. For transport assays of HEK293 cells overexpressed with *FLVCR1* or *FLVCR2* without co-
388 expressing with *CHKA* or *ETNK-1*, 20 μM [^{3}H] choline and 2.5 μM [^{14}C] ethanolamine was used.
389 For transport assays with indicated pH conditions, the following buffers were used: pH8.5 buffer (140
390 mM NaCl, 20 mM Tris-HCl pH 8.5, 2 mM $CaCl_2$, 1 g/L D-glucose), pH6.5 buffer (140 mM NaCl, 20 mM
391 MES pH 6.5, 2 mM $CaCl_2$, 1 g/L D-glucose), or pH7.5 buffer (140mM NaCl, 20mM HEPES-NaOH, 2mM
392 CaCl2, 1 g/L D-glucose). For sodium-free buffer, buffer containing 140 mM KCl, 20 mM HEPES-KOH pH
393 7.5, 2 mM $CaCl_2$, 1 g/L D-glucose was used. In these assays, 20 μM [^{3}H] choline or 2.5 μM [^{14}C]
394 ethanolamine was used, and the assays were stopped after 15 minutes of incubation with the ligands.
395 Radioactive signals from cell lysates were normalized to total protein levels.

396 **Immunofluorescent staining (IF)**

397 HEK293 cells were seeded onto 24-well plates with coverslips and maintained in Dulbecco's Modified
398 Eagle's Medium (Gibco) supplemented with 10% fetal bovine serum and 1% penicillin-streptomycin.
399 HEK293 cells were co-transfected with *FLVCR1* or *FLVCR2* with membrane expressing GFP (Addgene:
400 #14757) using Lipofectamine™ 2000 reagent (Thermo Fisher Scientific). The inducible HEK293 stable
401 cell lines overproducing FLVCR1 or FLVCR2 were seeded onto Millicell EZ SLIDE 8-well glass slides
402 (Merck), respectively. The stable cell lines were induced at 80% confluence by adding a final
403 concentration of 2 μg ml^{-1} doxycycline hydrochloride. The protein overproduction was carried out for
404 24 h. For permeabilization and staining, cells were washed with PBS twice and fixed in 4% PFA for 15
405 minutes at room temperature, followed by washing with PBS twice, and permeabilized in PBST (PBS
406 with 0.5% triton-X) for 15 minutes at room temperature. For immunofluorescent staining, the HEK293
407 cells were subsequently washed with PBS and blocked in 5% normal goat serum for one hour before
408 staining with FLVCR1 and FLVCR2 polyclonal antibodies at 1:250 dilutions for 1 h and then with alexa

409 Fluor 555 as secondary antibody at 1:500 dilutions for 1 h. The cells were counter-stained with DAPI
410 and imaged with laser confocal microscope (Zeiss LSM710). The overproduction stable cells were
411 treated with the same protocol but stained with Monoclonal ANTI-FLAG® M2-FITC antibody against
412 their FLAG-tags, and MitoTracker™ Red CMXRos for mitochondria localization. The cells were mounted
413 using ProLong™ Diamond mounting medium with DAPI and imaged with laser confocal microscope
414 (Confocal Microscope Leica STELLARIS 5).

415 **Structure-guided mutagenesis**

416 To generate the mutant plasmids for *FLVCR1* and *FLVCR2*, an overlapping PCR approach was used. The
417 mutated cDNA of *FLVCR1* or *FLVCR2* was cloned into pcDNA3.1 for overexpression. The mutations were
418 validated by Sanger sequencing. To test the transport activity of these mutants, the mutant plasmid
419 was either co-transfected with *CHKA* for choline transport assay or *ETNK-1* for ethanolamine transport
420 assay. After 24 hours of post-transfections, cells were washed with DMEM and incubated with DMEM
421 containing 20 μM [^{3}H] choline or 2.5 μM [^{14}C] ethanolamine for *FLVCR1* mutants and 100 μM [^{3}H]
422 choline or 2.5 μM [^{14}C] ethanolamine for *FLVCR2* mutants. The assays were stopped after 1 h of
423 incubation at 37 °C. Radioactive signal of each mutant was normalized to the total protein levels.

424 **Choline export assay**

425 To examine the export function, *FLVCR1* and *FLVCR2* plasmids were expressed in HEK293 cells without
426 co-transfection with *CHKA* or *ETNK-1*. The cells were then incubated with 200 μM [^{3}H] choline or 100
427 μM [^{14}C] ethanolamine for 2 hours to prepack the cells with the ligand. Subsequently, the cells were
428 washed to remove the ligands left over in the medium and incubated with choline/ethanolamine-free
429 medium for 1 h at 37 °C for the release of pre-packed ligand. The cells were washed and collected for
430 quantification of radioactive signals. Samples after 2 hours of incubation with the radioactive ligand
431 were collected to determine the levels of radioactive levels before the release and used for control.

432 **Hemin import assay**

433 For hemin import activity measurement, HEK293 cells were transfected with *FLVCR1* or *FLVCR2*. After
434 24 hours of transfection, cells were incubated with 2.5 μM [^{3}H] hemin in DMEM containing 10% FBS
435 for 1 h. The cells were then washed and collected for quantification of radioactive signals. For the

436 transport assays where hemin was co-incubated with radioactive ligands, HEK293 cells with
437 overexpression of *FLVCR2* were incubated with 50 μM hemin and 10 μM [^{3}H] choline or 20 μM hemin
438 and 2.5 μM [^{14}C] ethanolamine for 1 hour. Radioactive signals from the cells were quantified.

439 **Deglycosylation assay**

440 PNGase assay was performed on FLVCR1 and FLVCR2 proteins purified from HEK293 cells were treated
441 with PNGase (NEB). *FLVCR1* and *FLVCR2* expressed in Expi293T GnTi- cells were used for control.
442 Treated protein samples were then subjected to Western blot analysis.

443 **Metabolomic analysis**

444 Adult livers (aged 3-6 months old) from control (*FLVCR1*$^{f/f}$) and conditional *FLVCR1* knockout (*FLVCR1*$^{f/f}$
445 Mx1-Cre) mice were used for metabolomic analysis. Briefly, the mice were perfused with PBS to
446 remove blood before organ collection. Liver samples were snap-frozen before shipped for
447 metabolomics by Metabolon. The levels of metabolites were expressed as relative amount.

448 **Production and purification of the human FLVCR1 and FLVCR2.**

449 For protein production, the Flp-In T-REx293-FLVCR1 and Flp-In T-REx293-FLVCR2 cell lines were
450 cultured in roller bottles (Greiner Bio-One) in growth media containing 100 μg ml^{-1} hygromycin B for
451 14 d under the above-mentioned conditions. Gene expression was induced at 100% confluence by
452 adding a final concentration of 2 μg ml^{-1} doxycycline hydrochloride. After 72 h, cells were harvested
453 with Accutase solution (Sigma-Aldrich) and stored at −80 °C until further use. Harvested cells were
454 suspended in cold lysis buffer containing 25 mM Tris pH 7.4, 150 mM NaCl, and 0.1 g ml^{-1} SigmaFast
455 ethylenediaminetetraacetic acid (EDTA)-free protease inhibitor (Sigma-Aldrich) and disrupted by
456 stirring under high-pressure nitrogen atmosphere (750 MPa) for 45 min at 4 °C in a cell-disruption
457 vessel (Parr Instrument). The cell lysate was centrifuged at 8,000*g* at 4 °C for 15 min. Subsequently,
458 the low-velocity supernatant was centrifuged at 220,000*g* at 4 °C for 60 min. Pelleted membranes were
459 resuspended and stored in a storage buffer containing 25 mM Tris pH 7.4, 150 mM NaCl, 10% glycerol
460 (v/v), and 0.1 g ml^{-1} SigmaFast EDTA-free protease inhibitor (Sigma-Aldrich).

461 All purification steps of both FLVCRs were performed at 4 °C. Isolated membranes were solubilized
462 with 1% (w/v) lauryl maltose neopentyl glycol (LMNG; GLYCON Biochemicals) with gentle stirring for 1

463 h. The insoluble membrane fraction was removed via ultracentrifugation at 220,000*g* for 1 h.
464 Subsequently, the supernatant was incubated with ANTI-FLAG® M2 Affinity Gel resin (Merck) for 1 h.
465 The resin was preequilibrated with a buffer containing 50 mM Tris pH 7.4, 150 mM NaCl, and 0.02%
466 LMNG (w/v). The washing step was performed using 20 column volumes (CVs) of wash buffer [50 mM
467 Tris pH 7.4, 150 mM NaCl, 5% (v/v) glycerol, and 0.02% LMNG). The protein was eluted from the M2
468 resin with 10 CVs of the same buffer supplemented with 4 mM FLAG® Peptide (Merck). The eluted
469 sample was concentrated and subjected to a Superdex 200 Increase 10/300 column (GE Healthcare)
470 equilibrated with size exclusion chromatography (SEC) buffer [50 mM Tris pH 7.4, 150 mM NaCl, and
471 0.001% (w/v) LMNG]. Peak fractions were pooled, concentrated to 1.5 mg ml^{-1} using an Amicon 50-
472 kDa cut-off concentrator (Merck Millipore), and stored for further analysis.

473 **Immunoblotting**

474 Affinity-purified proteins were subjected to SDS-PAGE and immunoblotting. FLAG-tagged FLVCR1 and
475 FLVCR2 were detected using anti-FLAG (F3165, Sigma-Aldrich) antibodies at 1:1,000 dilution. Anti-
476 mouse IgG antibody conjugated with alkaline phosphatase (A9316, Sigma-Aldrich) was used as
477 secondary antibody at 1:5,000 dilution. Native FLVCR1 and FLVCR2 proteins were detected by
478 polyclonal FLVCR1 and FLVCR2 antibodies raised in-house at 1:1000 dilution. GAPDH antibody was
479 purchased from Santa Cruz.

480 **Tryptophan fluorescence measurement**

481 Tryptophan fluorescence measurements were carried out using Prometheus Panta (NanoTemper
482 Technologies). Purified protein samples were diluted with dilution buffer containing 50 mM HEPES pH
483 7.4, 150 mM NaCl, and 0.001% (w/v) LMNG to 1 μM. Buffers with different concentrations of choline
484 or betaine were prepared by serial dilutions of dilution buffer containing 4 mM of the compounds. The
485 protein samples were mixed with an equal volume of dilution buffer or the compound-containing
486 buffer with a final protein concentration of 0.5 μM and then incubated at room temperature for 15
487 min. A volume of 10 μl mixed solution was used per Prometheus high sensitivity capillary (NanoTemper
488 Technologies). Recorded F_{350}/F_{330} was analyzed by using Python libraries including pandas, numpy,

489 scipy and seaborn in Visual Studio Code (Microsoft). Three technical replicates were recorded for data
490 analysis.

491 **Cryo-EM sample preparation**

492 In order to collect cryo-EM data of FLVCR1 and FLVCR2 in different sample conditions, different
493 combinations of FLVCR proteins and putative substrate molecules were prepared. For both as-isolated
494 samples of FLVCRs, the protein concentration was adjusted to approximately 1.5 mg ml^{-1} and
495 subjected to plunge freezing. For samples supplemented with heme, heme loading was performed
496 prior to the SEC during protein purification with a 10-fold molar excess to the protein concentration.
497 Peak fractions were pooled and concentrated to 1.5 mg ml^{-1} before sample vitrification. For samples
498 supplemented with choline, purified proteins were adjusted to 1.5 mg ml^{-1} and choline was added at
499 a final concentration of 1 mM. The samples were incubated for 10 minutes at room temperature
500 before plunge freezing. Identical plunge freezing conditions were applied for all samples: Quantifoil
501 R1.2/1.3 copper grids (mesh 300) were washed in chloroform and subsequently glow-discharged with
502 a PELCO easiGlow device at 15 mA for 90 seconds. A volume of 4 µl sample was applied to a grid and
503 blotting was performed for 4 seconds at 4 °C, 100% humidity with nominal blot force 20 immediately
504 before freezing in liquid ethane, using a Vitrobot Mark IV device (Thermo Scientific).

505 **Cryo-EM image recording**

506 For each cryo-EM sample, a dataset was recorded in Energy-Filtered Transmission Electron Microscopy
507 (EF-TEM) mode using either a Titan Krios G3i or a Krios G4 microscope (Thermo Scientific), both
508 operated at 300 kV. Electron-optical alignments were adjusted with EPU 3.0 - 3.4 (Thermo Scientific).
509 Images were recorded using automation strategies of EPU 3.0 - 3.4 in electron counting mode with
510 either a Gatan K3 (installed on Krios G3i) or a Falcon4 (installed on Krios G4) direct electron detector.
511 For Gatan K3 detector, a nominal magnification of 105,000, corresponding to a calibrated pixel size of
512 0.837 Å was applied, and dose fractionated movies (80 frames) were recorded at an electron flux of
513 approximately 15 e^{-} x $pixel^{-1}$ x s^{-1} for 4 s, corresponding to a total dose of ~80 e^{-}/A^{2}. For Falcon4 detector,
514 a nominal magnification of 215,000, corresponding to a calibrated pixel size 0.573 Å was applied, dose
515 fractionated movies were recorded in electron-event representation (EER) format at an electron flux

516 of approximately 4 e^- x $pixel^{-1}$ x s^{-1} for 5 s, corresponding to a total dose of ~50 e^-/A^2. Images were
517 recorded between -1.1 and -2.0 µm nominal defocus. Data collection quality was monitored through
518 EPU v. 3.0-3.4 and CryoSparc Live (versions 3.0 and 4.0)[38].

519 **Cryo-EM image processing**

520 For each acquired dataset, the same cryo-EM image processing approach was applied: MotionCor2
521 was used to correct for beam-induced motion and to generate dose-weighted images[39]. Gctf was used
522 to determine the contrast transfer function (CTF) parameters and perform correction steps[40]. Images
523 with estimated poor resolution (>4 Å) and severe astigmatism (>400 Å) were removed at this step.
524 Particles were picked by TOPAZ and used for all further processing steps[41]. 2D classification, initial
525 model generation, 3D classification, CTF refinement, Bayesian polishing, 3D sorting, and final map
526 reconstructions were performed using RELION (versions 3.1 and 4.0) or cryoSPARC (versions 3.0 and
527 4.0)[38,42,43]. Fourier shell correlation (FSC) curves and local-resolution estimation were generated in
528 RELION or cryoSPARC for individual final maps. A schematic overview of our processing workflow, and
529 a summary of map qualities are shown in Supplementary Figs. 2, 3 and 9, and Supplementary Table 4.

530 **Model building and geometry refinement**

531 The first atomic model of FLVCR1 and FLVCR2 were built into the respective EM density maps of the
532 as-isolated state in Coot (version 0.8) or ISOLDE within ChimeraX (version 1.5 and 1.6)[44–46], using the
533 AlphaFold predicted structures as initial templates[47]. After manual backbone tracing and docking of
534 side chains, real-space refinement in Phenix was performed (version 1.18)[48]. Refinement results were
535 manually inspected and corrected if required. This model was used as a template to build all
536 subsequent atomic models. The finalized models were validated by MolProbity implemented in
537 Phenix[49]. Map-to-model cross-validation was performed in Phenix (version 1.18). $FSC_{0.5}$ was used as
538 cut-off to define resolution. A summary of model parameters and the corresponding cryo-EM map
539 statistics is found in Supplementary Table 4. The finalized models were visualized using ChimeraX. The
540 built models of both FLVCR proteins in different states were used as starting structures for MD
541 simulations.

542 **Molecular dynamics simulations**

543 All simulations were run using GROMACS 2022.4[50]. The protein structures were embedded in a lipid
544 bilayer with 75% POPE and 25% POPG with CHARMM-GUI[51] and solvated in TIP3P water with 150 mM
545 NaCl. The charmm36m force field[52] was used with the improved WYF parameter set for cation-pi
546 interactions[53]. Initial systems were minimized for 5000 steepest-descent steps and equilibrated for 250
547 ps of MD in an NVT ensemble and for 1.625 ns in an NPT ensemble. Position restraints of 4000 and
548 2000 kJ mol^{-1} nm^{-2} in the backbone and side chain heavy atoms, respectively, were gradually released
549 during equilibration. The z-positions of membrane phosphates, as well as lipid dihedrals, were initially
550 restrained with force constants of 1000 kJ mol^{-1} nm^{-2}, which were gradually released during
551 equilibration. The initial time step of 1 fs was increased to 2 fs during NPT equilibration. Long-range
552 electrostatic interactions were treated with particle-mesh Ewald (PME)[54] with a real-space cut-off of
553 1.2 nm. Van-der-Waals interactions were cut-off beyond a distance of 1.2 nm. The LINCS algorithm[55]
554 was used to constrain the bonds involving hydrogen atoms. During equilibration, a constant
555 temperature of 310 K was maintained with the Berendsen thermostat[56], using a coupling constant of
556 1 ps. Constant pressure of 1 bar was established with a semi-isotropic Berendsen barostat and a
557 coupling constant of 5 ps. In the production runs, a Nosé–Hoover thermostat[57] and a Parrinello–
558 Rahman barostat were used[58].
559 We used our cryo-EM structures as initial models for simulations of apo and choline-bound inward-
560 facing FLVCR1, apo and choline-bound inward-facing FLVCR2, and apo outward-facing FLVCR2. An
561 initial structure of choline-bound outward-facing FLVCR2 was generated aligning apo outward-facing
562 FLVCR2 to choline-bound inward-facing FLVCR2 and maintaining choline in the cavity. In choline entry
563 simulations, the apo structures were used with 380 mM choline in solution. For simulations of
564 ethanolamine-bound FLVCR1, the choline within the cavity of the cryo-EM structure was replaced by
565 this ligand. Simulations of heme-bound outward- and inward-facing FLVCR2 were prepared by
566 manually placing heme close to the observed binding region in the N-terminus of the apo structures,
567 outside of the lipid bilayer. Additionally, simulations of FLVCR2 in the outward-facing conformation
568 were conducted, with the heme initially positioned in front of the cavity entrance. Three replicas with
569 random initial velocities from the Boltzmann distribution were run for all systems. Choline release

570 simulations were interrupted after choline exit from the cavity, and hence have variable duration. For
571 all other systems, each replica was run for 1 µs.
572 Alanine substitution mutations were introduced using PyMol[59] and simulated with identical
573 parameters as those applied in the corresponding wild-type simulations. In FLVCR1, only one mutation
574 was introduced in the cavity residue W125. Mutations of FLVCR2 included the cavity residue W102
575 and the heme binding residues R82, R83 (simultaneously) and K273A.
576 Visual Molecular Dynamics (VMD)[60] and MDAnalysis[61] were used to visualize and analyze the
577 trajectories, respectively.
578 **Interior tunnels and cavities**
579 Tunnels and cavities were mapped with MOLE 2.5[62] with a bottleneck radius of 1.2 Å, bottleneck
580 tolerance 3 Å, origin radius 5 Å, surface radius 10 Å, probe radius 5 Å and an interior threshold of 1.1 Å.
581 We calculated the volume of the cavity using CASTp[63] with a bottleneck radius of 1.4 Å. Residues 297-
582 320 and 512-516 were removed from the FLVCR1 model to avoid the misattribution of the volume
583 between internal loops to the cavity volume. Analogously, residues 272-296 and 487-502 were not
584 included in the cavity volume calculation of FLVCR2.
585 **Multiple sequence alignments**
586 Multiple sequence alignments of FLVCR1 and FLVCR2 from *homo sapiens*, *Felis catus*, *Mus musculus*,
587 and *Sus scrofa* were performed using Clustal Omega[64].

588 **Data availability**

589 Cryo-EM maps are deposited at the Electron Microscopy Data Bank under accession numbers:EMD-
590 18334, EMD-18335, EMD-18336, EMD-18337, EMD-18338, EMD-18339, EMD-19009, EMD-19018.
591 Atomic models of human FLVCR1 and FLVCR2 have been deposited to the Protein Data Bank under
592 accession numbers: 8QCS, 8QCT, 8QCX, 8QCY, 8QCZ, 8QD0, 8R8T. All other data is presented in the
593 main text or supplementary materials. Source data are provided with this paper.

594

595 **Acknowledgements**

596 We thank Hartmut Michel for supporting and providing infrastructural resources. We thank the Central
597 Electron Microscopy Facility at MPI of Biophysics for technical support and access to instrumentation.

598

599 **Funding**

600 This work was supported by the Max Planck Society and the Nobel Laureate Fellowship of the Max
601 Planck Society (to D.W. and S.S.) and Singapore Ministry of Education T2EP30221-0012, T2EP30123-
602 0014, NUHSRO/2022/067/T1 grants (to L.N.N.).

603

604 **Author contributions**

605 T-H.W. purified proteins, performed biochemical assays, prepared grids, collected cryo-EM data,
606 processed cryo-EM data, refined the structure, built the model, co-drafted the manuscript, and
607 prepared figures. K.R., Z.Y., and T.J.Y. L. performed mutagenesis. K.R. performed transport assays and
608 WB for mutants, and export assays. N.C.P.L. and Z.Y. performed dose curve, time course, and
609 glycosylation assay, and immunostaining. A.C.C. performed MD simulations, analyzed data, co-drafted
610 the manuscript, and prepared figures. W.J. performed cell productions, optimized purification
611 conditions, and purified proteins. A.B. performed assays and analyzed data. R.T.D and J.L.A designed
612 and performed animal model experiments. S.W. calibrated and aligned the microscope. G.G.
613 performed IF assays and protein purification. S.L.S performed protein purification. G.H., D.W., L.N.N.,
614 and S.S. supervised the project. D.W. implemented cell production and protein purification, prepared
615 grids, performed initial cryo-EM screening experiments, collected cryo-EM data, analyzed data, drafted
616 the manuscript, generated figures, and funded the project. L.N.N. designed functional assays,
617 interpreted, analyzed data, funded the project, and co-drafted the manuscript. D.W. and S.S. initiated
618 the project. S.S. designed research, evaluated data, funded the project, drafted the manuscript, and
619 generated figures.

620

621 **Competing interests**

622 The authors declare no conflict-of-interest

623 **References**

624 1. Khan, A. A. & Quigley, J. G. Heme and FLVCR-related transporter families SLC48 and SLC49. *Mol.*
625 *Asp. Med.* **34**, 669–682 (2013).
626 2. Rajadhyaksha, A. M. *et al.* Mutations in FLVCR1 Cause Posterior Column Ataxia and Retinitis
627 Pigmentosa. *Am. J. Hum. Genet.* **87**, 643–654 (2010).
628 3. Shaibani, A., Wong, L.-J., Zhang, V. W., Lewis, R. A. & Shinawi, M. Autosomal recessive posterior
629 column ataxia with retinitis pigmentosa caused by novel mutations in the FLVCR1 gene. *Int. J.*
630 *Neurosci.* **125**, 43–49 (2015).
631 4. Chiabrando, D. *et al.* Mutations in the Heme Exporter FLVCR1 Cause Sensory Neurodegeneration
632 with Loss of Pain Perception. *PLoS Genet.* **12**, e1006461 (2016).
633 5. Lischka, A. *et al.* Genetic landscape of congenital insensitivity to pain and hereditary sensory and
634 autonomic neuropathies. *Brain* **146**, 4880–4890 (2023).
635 6. Meyer, E. *et al.* Mutations in FLVCR2 Are Associated with Proliferative Vasculopathy and
636 Hydranencephaly-Hydrocephaly Syndrome (Fowler Syndrome). *Am. J. Hum. Genet.* **86**, 471–478
637 (2010).
638 7. Thomas, S. *et al.* High-throughput sequencing of a 4.1 Mb linkage interval reveals FLVCR2 deletions
639 and mutations in lethal cerebral vasculopathy. *Hum. Mutat.* **31**, 1134–1141 (2010).
640 8. Quigley, J. G. *et al.* Identification of a Human Heme Exporter that Is Essential for Erythropoiesis.
641 *Cell* **118**, 757–766 (2004).
642 9. Keel, S. B. *et al.* A Heme Export Protein Is Required for Red Blood Cell Differentiation and Iron
643 Homeostasis. *Science* **319**, 825–828 (2008).
644 10. Yang, Z. *et al.* Kinetics and Specificity of Feline Leukemia Virus Subgroup C Receptor (FLVCR)
645 Export Function and Its Dependence on Hemopexin*. *J. Biol. Chem.* **285**, 28874–28882 (2010).
646 11. Doty, R. T. *et al.* Coordinate expression of heme and globin is essential for effective
647 erythropoiesis. *J. Clin. Investig.* **125**, 4681–4691 (2015).
648 12. Fiorito, V. *et al.* The heme synthesis-export system regulates the tricarboxylic acid cycle flux and
649 oxidative phosphorylation. *Cell Rep.* **35**, 109252 (2021).
650 13. Duffy, S. P. *et al.* The Fowler Syndrome-Associated Protein FLVCR2 Is an Importer of Heme. *Mol.*
651 *Cell. Biol.* **30**, 5318–5324 (2010).
652 14. Yuan, X., Protchenko, O., Philpott, C. C. & Hamza, I. Topologically Conserved Residues Direct
653 Heme Transport in HRG-1-related Proteins*. *J. Biol. Chem.* **287**, 4914–4924 (2012).
654 15. Ponka, P., Sheftel, A. D., English, A. M., Bohle, D. S. & Garcia-Santos, D. Do Mammalian Cells
655 Really Need to Export and Import Heme? *Trends Biochem. Sci.* **42**, 395–406 (2017).
656 16. Li, Y. *et al.* MFSD7C switches mitochondrial ATP synthesis to thermogenesis in response to heme.
657 *Nat. Commun.* **11**, 4837 (2020).
658 17. Dutt, S., Hamza, I. & Bartnikas, T. B. Molecular Mechanisms of Iron and Heme Metabolism. *Annu.*
659 *Rev. Nutr.* **42**, 311–335 (2022).
660 18. Tailor, C. S., Willett, B. J. & Kabat, D. A putative cell surface receptor for anemia-inducing feline
661 leukemia virus subgroup C is a member of a transporter superfamily. *J. Virol.* **73**, 6500–5 (1999).
662 19. Brown, J. K., Fung, C. & Tailor, C. S. Comprehensive Mapping of Receptor-Functioning Domains in
663 Feline Leukemia Virus Subgroup C Receptor FLVCR1. *J. Virol.* **80**, 1742–1751 (2006).
664 20. Petrillo, S. *et al.* Endothelial cells require functional FLVCR1a during developmental and adult
665 angiogenesis. *Angiogenesis* 1–20 (2023) doi:10.1007/s10456-023-09865-w.
666 21. Santander, N. *et al.* Lack of Flvcr2 impairs brain angiogenesis without affecting the blood-brain
667 barrier. *J. Clin. Investig.* **130**, 4055–4068 (2020).
668 22. Peng, C. *et al.* FLVCR1 promotes the proliferation and tumorigenicity of synovial sarcoma through
669 inhibiting apoptosis and autophagy. *Int. J. Oncol.* **52**, 1559–1568 (2018).
670 23. Su, X. *et al.* The prognostic marker FLVCR2 associated with tumor progression and immune
671 infiltration for acute myeloid leukemia. *Front. Cell Dev. Biol.* **10**, 978786 (2022).
672 24. Kenny, T. C. *et al.* Integrative genetic analysis identifies FLVCR1 as a plasma-membrane choline
673 transporter in mammals. *Cell Metab.* **35**, 1057-1071.e12 (2023).

674 25. Ha, H. T. T. *et al.* Mfsd7b facilitates choline transport and missense mutations affect choline
675 transport function. *Cell. Mol. life Sci. : CMLS* **81**, 3 (2023).
676 26. Nguyen, X. T. A. *et al.* MFSD7c functions as a transporter of choline at the blood-brain barrier.
677 *bioRxiv* 2023.10.03.560597 (2023) doi:10.1101/2023.10.03.560597.
678 27. Geisler, C. E. *et al.* Hepatocyte membrane potential regulates serum insulin and insulin sensitivity
679 by altering hepatic GABA release. *Cell Rep.* **35**, 109298 (2021).
680 28. Yan, N. Structural Biology of the Major Facilitator Superfamily Transporters. *Annu. Rev. Biophys.*
681 **44**, 257–283 (2015).
682 29. Kalailingam, P. *et al.* Deficiency of MFSD7c results in microcephaly-associated vasculopathy in
683 Fowler syndrome. *J. Clin. Investig.* **130**, 4081–4093 (2020).
684 30. Naoe, Y. *et al.* Crystal structure of bacterial haem importer complex in the inward-facing
685 conformation. *Nat Commun* **7**, 13411 (2016).
686 31. Woo, J.-S., Zeltina, A., Goetz, B. A. & Locher, K. P. X-ray structure of the Yersinia pestis heme
687 transporter HmuUV. *Nat Struct Mol Biol* **19**, 1310–1315 (2012).
688 32. Wu, D. *et al.* Dissecting the conformational complexity and mechanism of a bacterial heme
689 transporter. *Nat. Chem. Biol.* **19**, 992–1003 (2023).
690 33. Drew, D., North, R. A., Nagarathinam, K. & Tanabe, M. Structures and General Transport
691 Mechanisms by the Major Facilitator Superfamily (MFS). *Chem. Rev.* **121**, 5289–5335 (2021).
692 34. Hediger, M. A., Clémençon, B., Burrier, R. E. & Bruford, E. A. The ABCs of membrane transporters
693 in health and disease (SLC series): Introduction☆☆☆. *Mol. Asp. Med.* **34**, 95–107 (2013).
694 35. Lin, L., Yee, S. W., Kim, R. B. & Giacomini, K. M. SLC transporters as therapeutic targets: emerging
695 opportunities. *Nat. Rev. Drug Discov.* **14**, 543–560 (2015).
696 36. Yaffe, D., Forrest, L. R. & Schuldiner, S. The ins and outs of vesicular monoamine transporters. *J.*
697 *Gen. Physiol.* **150**, 671–682 (2018).
698 37. Klingenberg, M. Ligand−Protein Interaction in Biomembrane Carriers. The Induced Transition Fit
699 of Transport Catalysis †. *Biochemistry* **44**, 8563–8570 (2005).
700 38. Punjani, A., Rubinstein, J. L., Fleet, D. J. & Brubaker, M. A. cryoSPARC: algorithms for rapid
701 unsupervised cryo-EM structure determination. *Nat. Methods* **14**, 290–296 (2017).
702 39. Zheng, S. Q. *et al.* MotionCor2: anisotropic correction of beam-induced motion for improved
703 cryo-electron microscopy. *Nat. Methods* **14**, 331–332 (2017).
704 40. Zhang, K. Gctf: Real-time CTF determination and correction. *J. Struct. Biol.* **193**, 1–12 (2016).
705 41. Bepler, T. *et al.* Positive-unlabeled convolutional neural networks for particle picking in cryo-
706 electron micrographs. *Nat. methods* **16**, 1153–1160 (2019).
707 42. Scheres, S. H. W. RELION: Implementation of a Bayesian approach to cryo-EM structure
708 determination. *J. Struct. Biol.* **180**, 519–530 (2012).
709 43. Kimanius, D., Dong, L., Sharov, G., Nakane, T. & Scheres, S. H. W. New tools for automated cryo-
710 EM single-particle analysis in RELION-4.0. *Biochem. J.* **478**, 4169–4185 (2021).
711 44. Emsley, P., Lohkamp, B., Scott, W. G. & Cowtan, K. Features and development of Coot. *Acta*
712 *Crystallogr. Sect. D* **66**, 486–501 (2010).
713 45. Croll, T. I. ISOLDE: a physically realistic environment for model building into low-resolution
714 electron-density maps. *Acta Crystallogr. Sect. D, Struct. Biol.* **74**, 519–530 (2018).
715 46. Goddard, T. D. *et al.* UCSF ChimeraX: Meeting modern challenges in visualization and analysis:
716 UCSF ChimeraX Visualization System. *Protein Sci.* **27**, 14–25 (2017).
717 47. Jumper, J. *et al.* Highly accurate protein structure prediction with AlphaFold. *Nature* **596**, 583–
718 589 (2021).
719 48. Adams, P. D. *et al.* PHENIX: a comprehensive Python-based system for macromolecular structure
720 solution. *Acta Crystallogr. Sect. D, Biol. Crystallogr.* **66**, 213–21 (2009).
721 49. Chen, V. B. *et al.* MolProbity: all-atom structure validation for macromolecular crystallography.
722 *Acta Crystallogr. Sect. D: Biol. Crystallogr.* **66**, 12–21 (2010).
723 50. Abraham, M. J. *et al.* GROMACS: High performance molecular simulations through multi-level
724 parallelism from laptops to supercomputers. *SoftwareX* **1**, 19–25 (2015).
725 51. Jo, S., Kim, T., Iyer, V. G. & Im, W. CHARMM-GUI: A web-based graphical user interface for
726 CHARMM. *J. Comput. Chem.* **29**, 1859–1865 (2008).

52. Huang, J. *et al.* CHARMM36m: an improved force field for folded and intrinsically disordered proteins. *Nat. Methods* **14**, 71–73 (2017).
53. Khan, H. M., MacKerell, A. D. & Reuter, N. Cation-π Interactions between Methylated Ammonium Groups and Tryptophan in the CHARMM36 Additive Force Field. *J. Chem. theory Comput.* **15**, 7–12 (2018).
54. Essmann, U. *et al.* A smooth particle mesh Ewald method. *J. Chem. Phys.* **103**, 8577–8593 (1995).
55. Hess, B., Bekker, H., Berendsen, H. J. C. & Fraaije, J. G. E. M. LINCS: A linear constraint solver for molecular simulations. *Journal of Computational Chemistry* (1997).
56. Berendsen, H. J. C., Postma, J. P. M., Gunsteren, W. F. van, DiNola, A. & Haak, J. R. Molecular dynamics with coupling to an external bath. *J. Chem. Phys.* **81**, 3684–3690 (1984).
57. Evans, D. J. & Holian, B. L. The Nose–Hoover thermostat. *J. Chem. Phys.* **83**, 4069–4074 (1985).
58. Parrinello, M. & Rahman, A. Polymorphic transitions in single crystals: A new molecular dynamics method. *J. Appl. Phys.* **52**, 7182–7190 (1981).
59. Schrödinger & LLC. The PyMOL Molecular Graphics System, Version 2.0. (2015).
60. Humphrey, W., Dalke, A. & Schulten, K. VMD: Visual molecular dynamics. *J. Mol. Graph.* **14**, 33–38 (1996).
61. Michaud-Agrawal, N., Denning, E. J., Woolf, T. B. & Beckstein, O. MDAnalysis: a toolkit for the analysis of molecular dynamics simulations. *J. Comput. Chem.* **32**, 2319–27 (2010).
62. Sehnal, D. *et al.* MOLE 2.0: advanced approach for analysis of biomacromolecular channels. *J. Cheminformatics* **5**, 39–39 (2013).
63. Tian, W., Chen, C., Lei, X., Zhao, J. & Liang, J. CASTp 3.0: computed atlas of surface topography of proteins. *Nucleic Acids Res.* **46**, W363–W367 (2018).
64. Sievers, F. *et al.* Fast, scalable generation of high-quality protein multiple sequence alignments using Clustal Omega. *Mol. Syst. Biol.* **7**, 539–539 (2011).

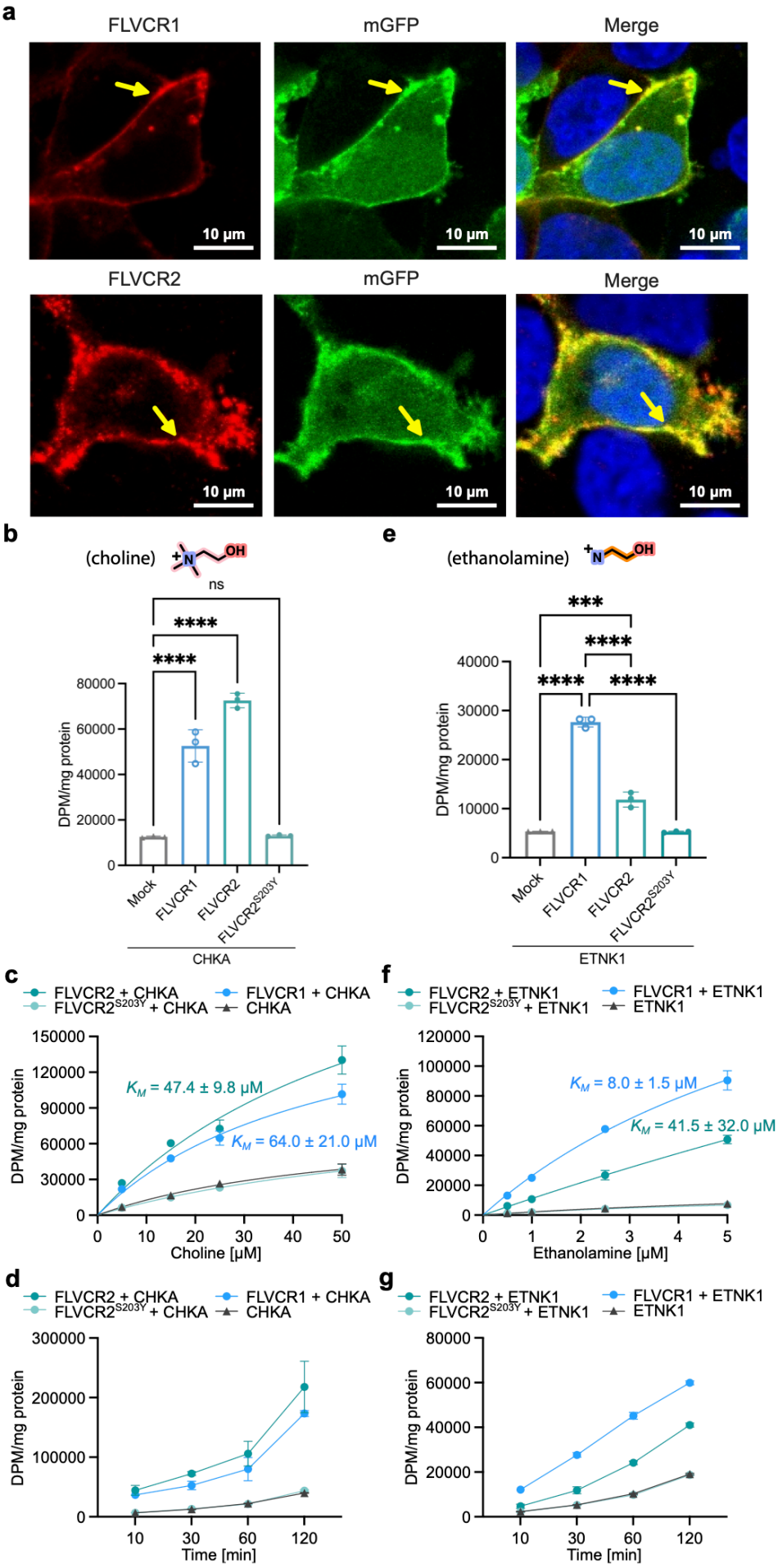
a
FLVCR1
mGFP
Merge
10 µm
FLVCR2
b
(choline)
ns
****
DPM/mg protein
Mock
FLVCR1
FLVCR2
FLVCR2S203Y
CHKA
e
(ethanolamine)
***
ETNK1
c
FLVCR2 + CHKA
FLVCR2S203Y + CHKA
FLVCR1 + CHKA
CHKA
KM = 47.4 ± 9.8 µM
KM = 64.0 ± 21.0 µM
Choline [µM]
f
FLVCR2 + ETNK1
FLVCR2S203Y + ETNK1
FLVCR1 + ETNK1
ETNK1
KM = 8.0 ± 1.5 µM
KM = 41.5 ± 32.0 µM
Ethanolamine [µM]
d
Time [min]
g

752

753 **Fig. 1: FLVCR1 and FLVCR2 are choline and ethanolamine transporters.**

754 **a**, Confocal imaging shows that FLVCR1 and FLVCR2 are localized at the plasma membrane (arrows). Plasma
755 membrane GFP (mGFP) was used as a marker. **b**, Choline transport activities of human FLVCR1 and FLVCR2.
756 Choline kinase A (*CHKA*) was co-expressed with both proteins. **b**,**c**, Dose curves and time courses for choline
757 transport activities of human FLVCR1 and FLVCR2. *CHKA* was co-expressed with both proteins. **d**, Ethanolamine
758 transport activities of human FLVCR1 and FLVCR2. Ethanolamine kinase 1 (*ETNK-1*) was co-expressed with both
759 proteins. **e**,**f**, Dose curves and time courses for ethanolamine transport activities of human FLVCR1 and FLVCR2.
760 *ETNK-1* was co-expressed with both proteins. The inactive S203Y mutant of FLVCR2 was used as a control in all
761 experiments. Each symbol represents one replicate. Data are expressed as mean ± SD. ****P<0.0001,
762 ***P<0.001. ns, not significant. One-way ANOVA for transport activity measurement; Two-way ANOVA for dose
763 curve measurements.

764

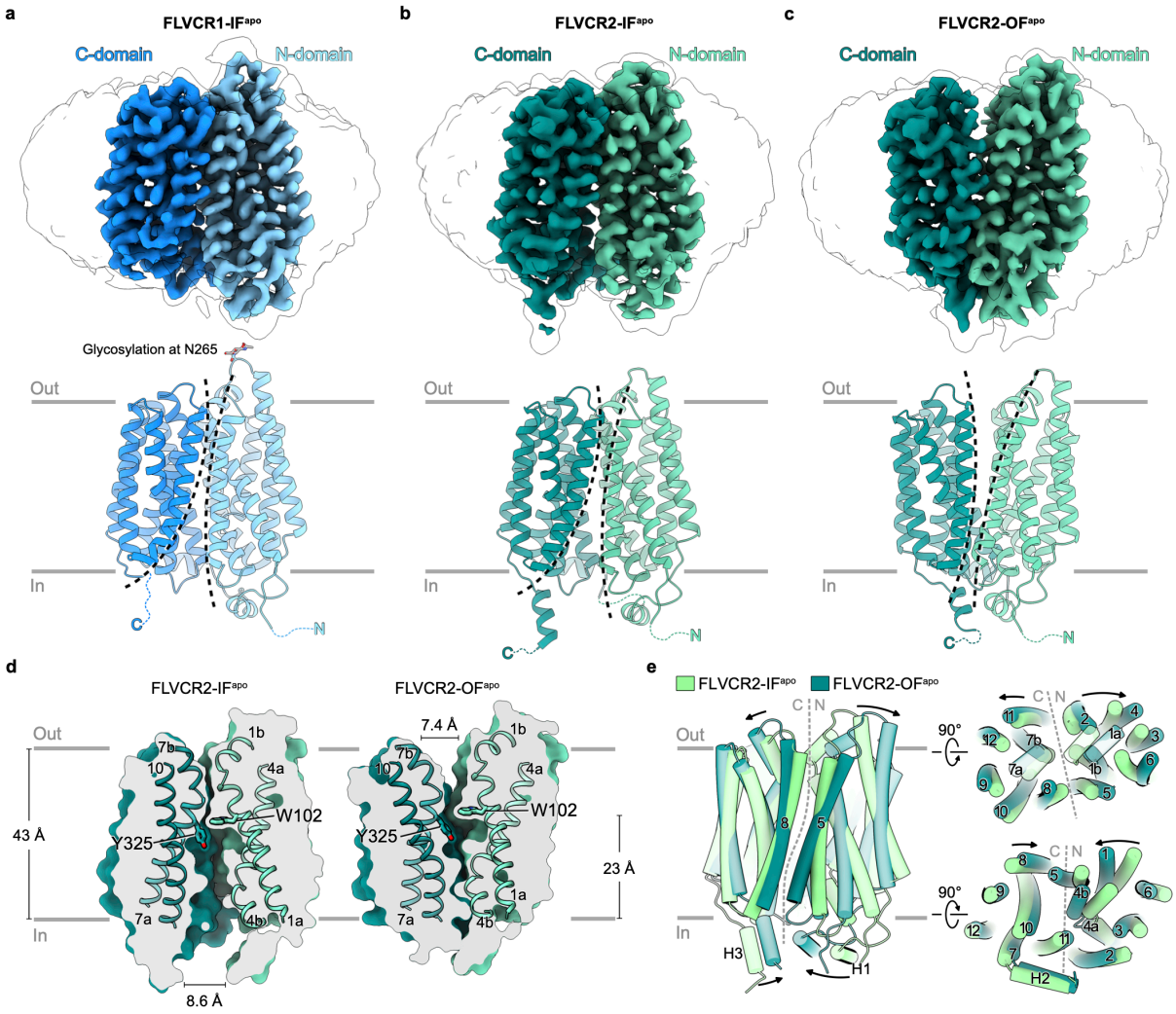

765

766 **Fig. 2: Architecture of FLVCR1 and FLVCR2 in their inward- and outward-facing states.**

767 Cryo-EM density (top) and atomic model (middle and bottom) of apo inward-facing FLVCR1 (**a**) as well as FLVCR2

768 in the inward-facing (**b**) and outward-facing (**c**) states. The N- and C-domains are coloured in different shades of

769 blue and green for FLVCR1 and FLVCR2, respectively. A transparent cryo-EM density lowpass-filtered at 6 Å is

770 shown to visualize the detergent belt surrounding the transmembrane region. The sidechain of N265 in FLVCR1

771 and its N-linked glycan (grey) are shown as stick models. **d**, Cut-away views of the surface representation showing

772 the cavity shape of FLVCR2-IF^{apo} (left) and FLVCR2-OF^{apo} (right). Two central aromatic residues are shown as sticks.

773 **e**, Structural superposition of FLVCR2-OF^{apo} (dark green) and FLVCR2-IF^{apo} (light green).

774

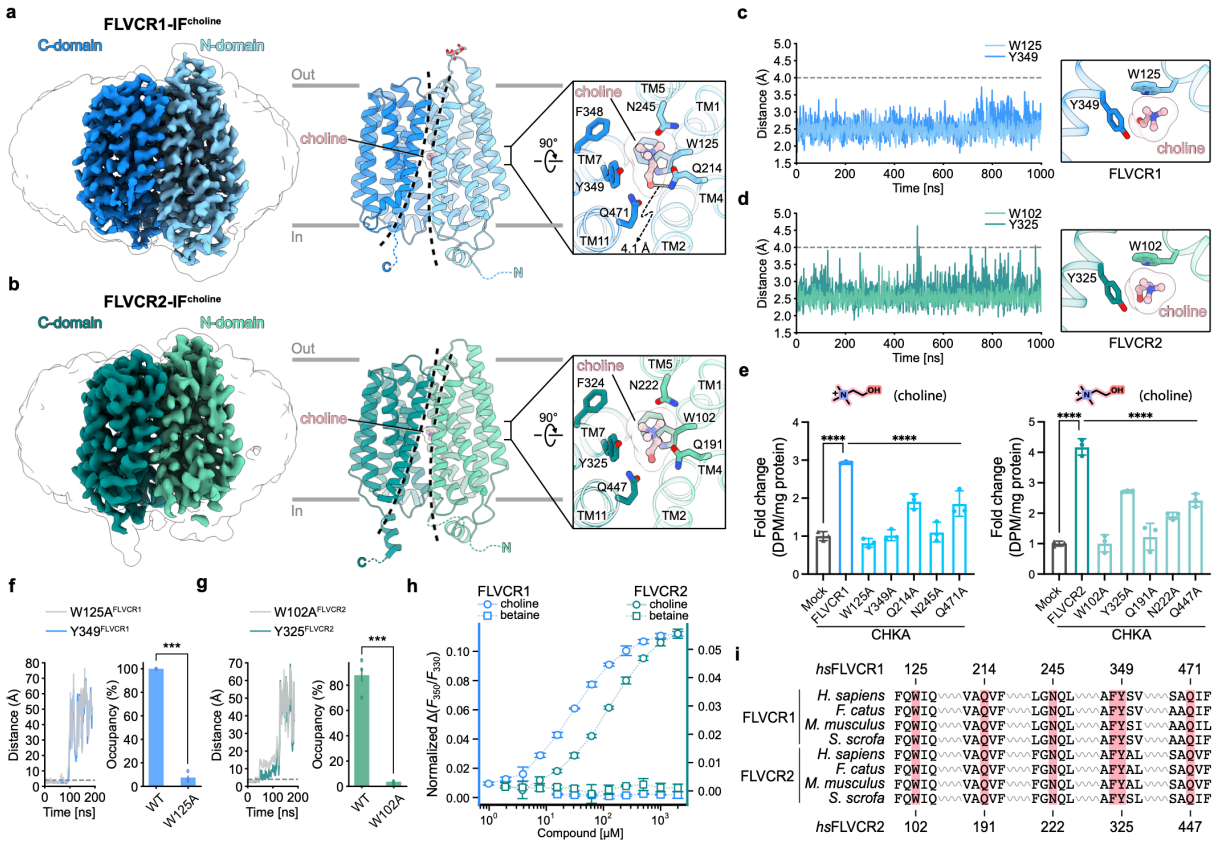

Fig. 3: Cryo-EM structures of FLVCR1 and FLVCR2 in complex with choline.

a,**b**, Cryo-EM densities and atomic models of the choline-bound inward-facing FLVCR1 (FLVCR1-IF^{choline}) structure (**a**), and the choline-bound inward-facing FLVCR2 (FLVCR2-IF^{choline}) structure (**b**), respectively. The bound choline is shown as ball-and-stick model; binding site residues are shown as sticks. **c**,**d**, Time-resolved distance plots between choline and the highly-conserved tryptophan and tyrosine residues forming the choline-binding pockets of FLVCR1 (**c**) and FLVCR2 (**d**) obtained from MD simulation runs. A cation-π interaction is assumed for distance < 4 Å (grey dashed line). **e**, Choline transport activity of indicated FLVCR1 and FLVCR2 mutants. *CHKA* was co-expressed with all proteins. 20 μM [^{3}H] choline was used for FLVCR1 mutants and 100 μM [^{3}H] choline was used FLVCR2 mutants, respectively. Each symbol represents one replicate. Mutant transport activities were normalized to the total protein from cells and displayed as fold change with reference to mock (empty vector). **f**,**g**, Distance of choline to conserved aromatics for W125A^{FLVCR1} (**f**) and W102A^{FLVCR2} (**g**) as function of time in MD simulations (left), and choline occupancy in binding site for WT and alanine mutants (right). Error bars represent standard errors of the mean (s.e.m.) **h**, Shifts of tryptophan fluorescence of FLVCR1 and FLVCR2 in the presence of choline or betaine. **i**, Protein sequence alignment of choline-binding pocket residues (red block) in FLVCR1 and FLVCR2 across various mammalian species. Indicated residue numbers refer to FLVCR1 and FLVCR2 from *homo*

791 *sapiens*. Data shown are mean ± SD for (**e**) and (**h**), and mean ± standard error of the mean (s.e.m) for (**f**).

792 ****P<0.0001, ***P<0.001. One-way ANOVA for (**e**), and *t*-test for (**f**) and (**g**).

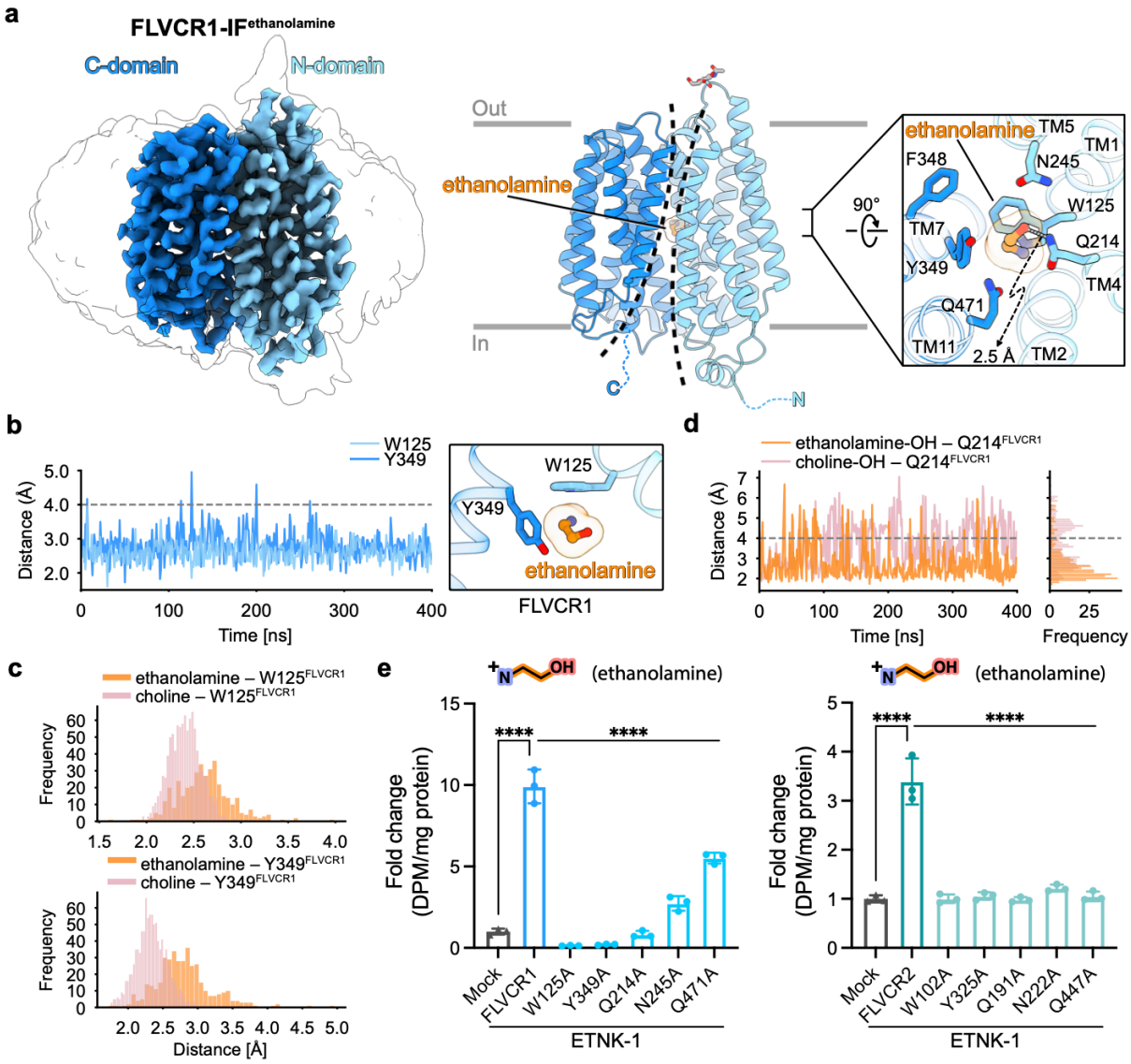

Fig. 4: Cryo-EM structures of FLVCR1 and FLVCR2 in complex with ethanolamine.

a, Cryo-EM density and atomic model of the ethanolamine-bound inward-facing FLVCR1 (FLVCR1-IF^{ethanolamine}) structure. The bound ethanolamine is shown as ball-and-stick model; binding site residues are shown as sticks. **b**, Distance of ethanolamine to conserved aromatics of FLVCR1 as function of time in MD simulation (left) and snapshot (right). **c**, Frequency of distance between ethanolamine or choline and W125^{FLVCR1} (top) or Y349^{FLVCR1} (bottom) derived from Fig. 3c and 4b, respectively. **d**, Distance between Q214^{FLVCR1} and the hydroxyl group of ethanolamine (orange) or choline (pink) as function of time in MD simulation, with corresponding frequency (right). **e**, Ethanolamine transport activities of indicated FLVCR1 and FLVCR2 mutants. *ETNK-1* was co-expressed with all proteins. 2.5 µM [^{14}C] ethanolamine was used. Transport activities of mutant variants were normalized to the total protein from cells and are displayed as fold change to mock (empty vector). Each symbol represents one replicate. Data shown are mean ± SD. ****P<0.0001. One-way ANOVA.

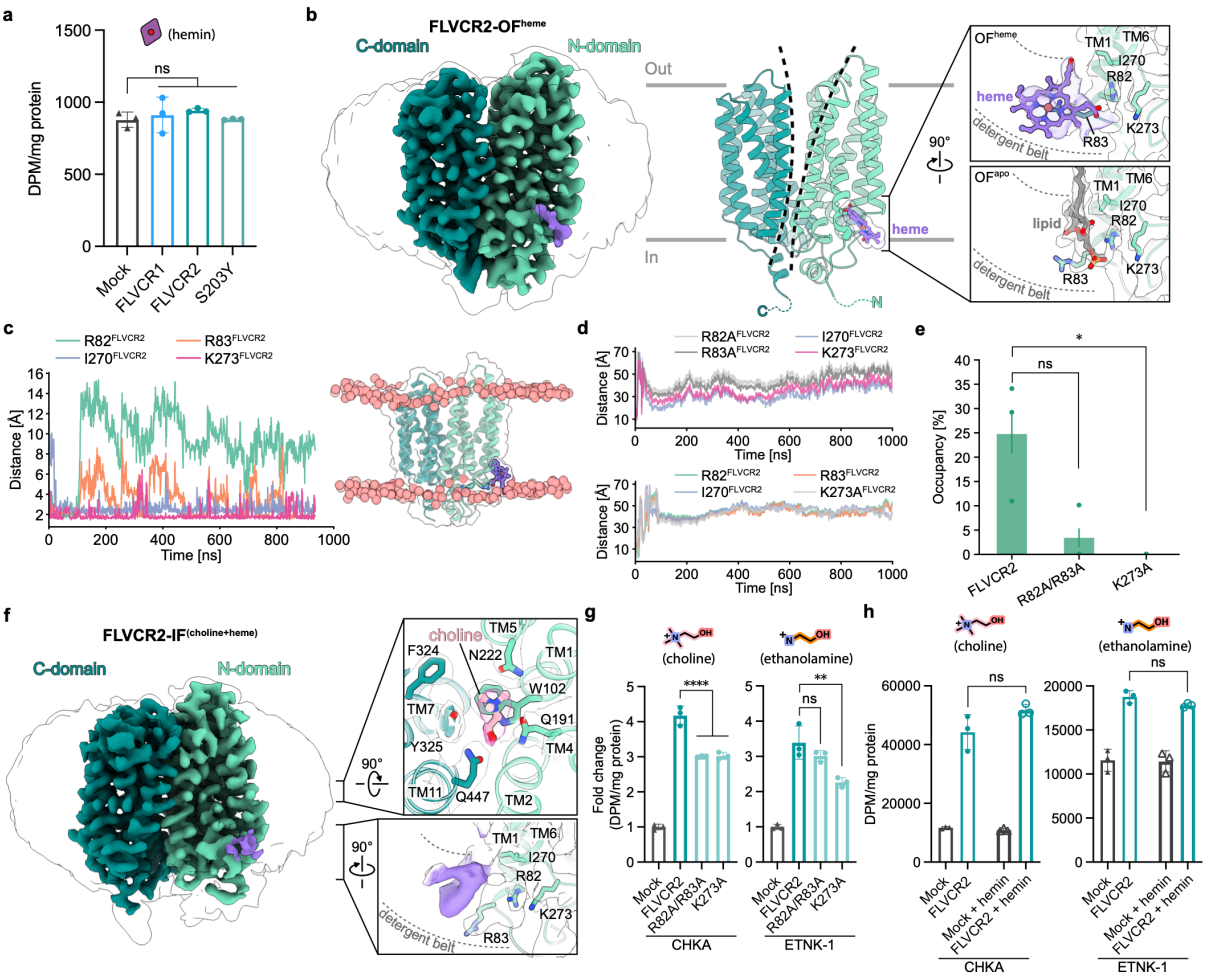

Fig. 5: Cryo-EM structures of FLVCR2 in complex with heme.

a, Import assay of FLVCR1 and FLVCR2 for heme. 2.5 µM [^{3}H] hemin was used. The inactive mutant of FLVCR2^{S203Y} was used as a control. **b**, Cryo-EM density (left) and ribbon model (right) of the heme-bound outward-facing FLVCR2 (FLVCR2-OF^{heme}). The heme molecule is shown in ball-and-stick representation, and the corresponding cryo-EM density is coloured in purple. Right panels are the close-up views of the heme-binding site in FLVCR2-OF^{heme} (top) and in FLVCR2-OF^{apo} (bottom) with locally-filtered cryo-EM density. Residues in close proximity to heme are shown as sticks. A lipid molecule (grey ball-and-stick) is fitted into the lipid-like density at the heme-binding site of FLVCR2-OF^{apo}. **c**, Distance of heme and interacting residues as function of time in MD simulations (left), with a snapshot of FLVCR2-heme interactions (right) indicating the membrane layer by the phosphates of POPE/POPG (red spheres). **d**, Distances as in (**c**, left), but for mutants R82A/R83A (top) and K273A (bottom). **e**, Interaction frequency of heme with four heme-interacting residues for WT and mutants of FLVCR2. **f**, Cryo-EM density of the heme-bound, choline-bound, inward-facing FLVCR2. The cryo-EM density corresponding to heme is coloured in purple. Right panels are the cryo-EM density of the substrate-binding site (top) and heme-binding site (bottom) in FLVCR2-IF$^{heme\text{-}choline}$ with rigid-body fitting of the FLVCR2-IF^{choline} model. The heme-binding site is

820 shown with locally-filtered cryo-EM density. **g**, Choline (left) and ethanolamine (right) transport assays for
821 *FLVCR2* heme-binding site mutants. *CHKA* or *ETNK-1* was co-expressed with WT or *FLVCR2* mutant plasmids. 100
822 μM [^{3}H] choline or 2.5 μM [^{14}C] ethanolamine was used, respectively. Transport activity of the mutants was
823 normalized to the total protein and is displayed as fold change to mock (empty vector). **h**, Choline (left) and
824 ethanolamine (right) transport assay for FLVCR2 in the presence of heme. For choline + hemin experiment, 10
825 μM [^{3}H] choline and 50 μM hemin were used, while for ethanolamine + hemin experiment, 2.5 μM [^{14}C]
826 ethanolamine and 25 μM hemin were used. The experiment was repeated twice for (**a**). One dataset was shown.
827 Each symbol represents one replicate. Data are expressed as mean ± SD for (**a**), (**g**) and (**h**), and mean ± s.e.m for
828 (**e**). ****P<0.0001, **P<0.01, *P<0.05. ns, not significant. One-way ANOVA for (**a**) and (**g**), two-way ANOVA for
829 (**h**), and *t*-test for (**e**).
830

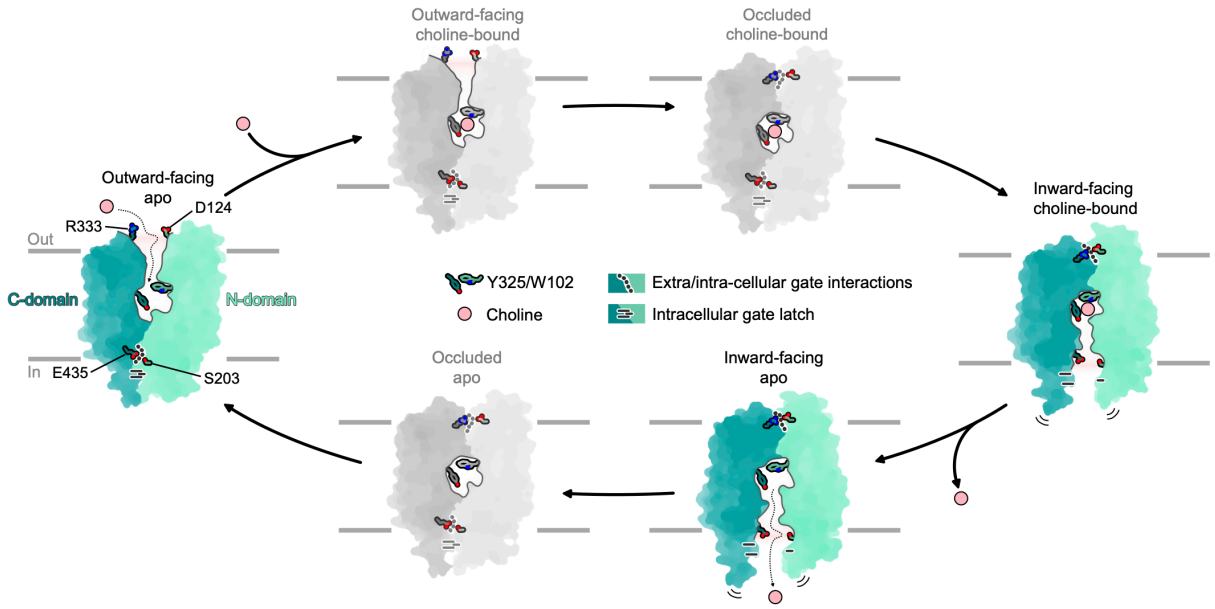

Fig. 6: Proposed model for choline transport by FLVCR2.

Schematic illustration of FLVCR2 conformations during the choline transport cycle. Green-colored states represent experimentally obtained conformations of this study. States colored in grey are hypothesized based on knowledge about the commonly characterized alternative-access mechanism of MFS transporters.

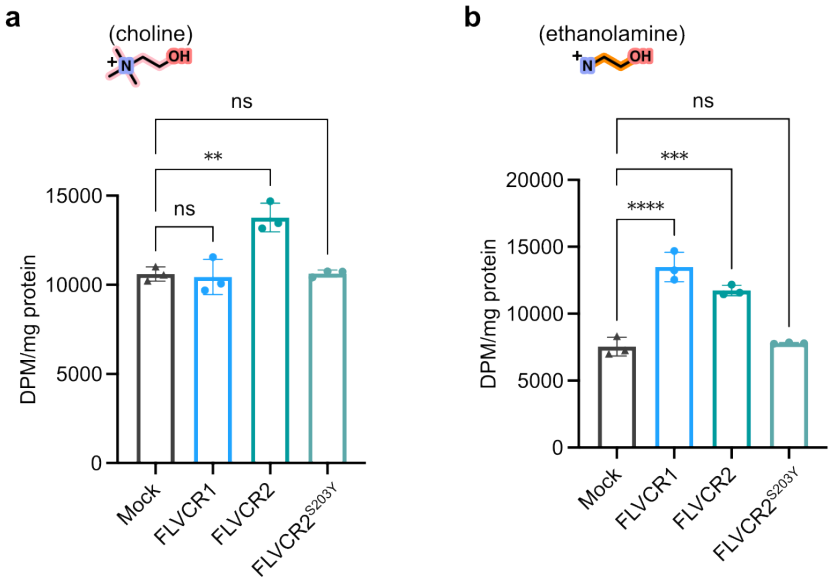

Extended Data Fig. 1: Transport activity of FLVCRs for choline or ethanolamine without overexpression of *CHKA* or *ETNK-1*.

Choline (**a**) or ethanolamine (**b**) transport activity of FLVCR1, FLVCR2, and FLVCR2^{S203Y} without simultaneous overexpression of *CHKA* or *ETNK-1*, respectively. 20μM [^{3}H] choline or 2.5μM [^{14}C] ethanolamine was used, respectively. The inactive mutant of FLVCR2^{S203Y} was used as a control in all experiments. Each experiment was repeated twice and one dataset was shown. Each symbol represents one replicate. Data are expressed as mean ± SD. ****P<0.0001, ***P<0.001, **P<0.01. ns, not significant. One-way ANOVA.

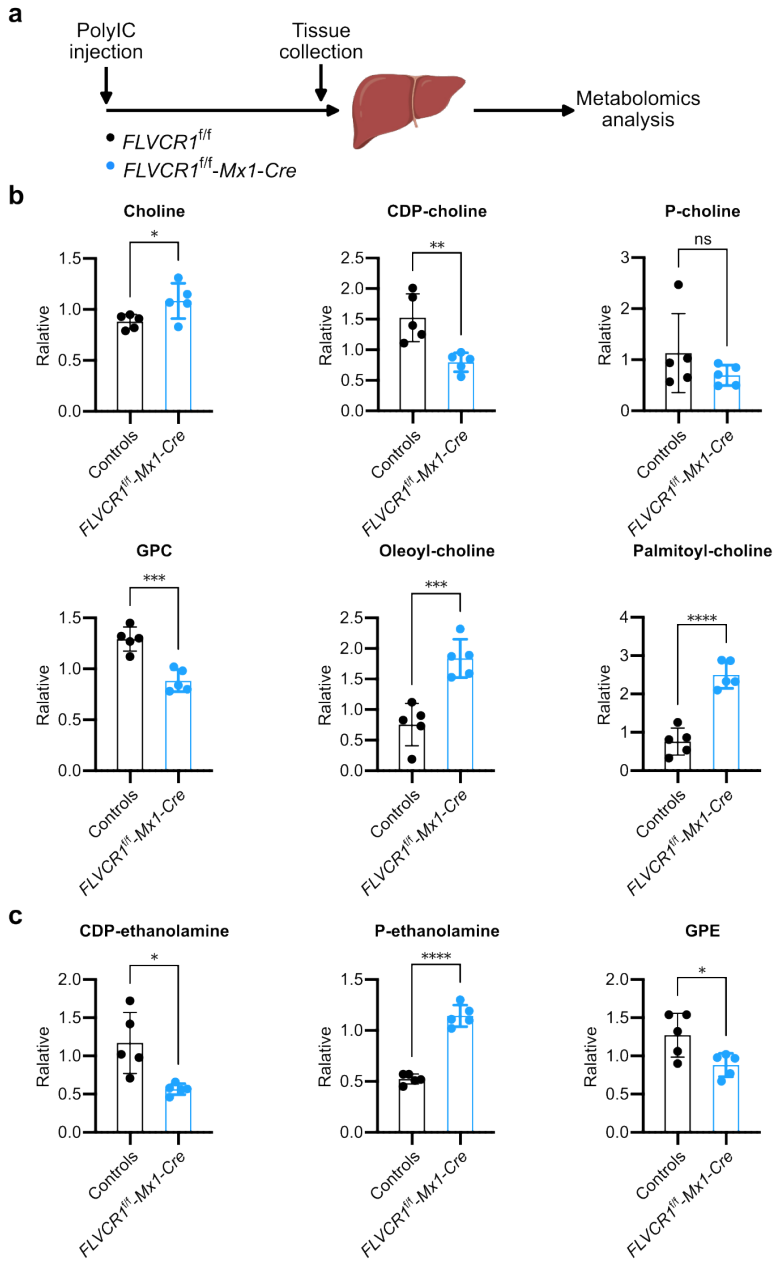

848

849 **Extended Data Fig. 2: Metabolomic analysis of livers from *FLVCR1*-knockout mice.**

850 **a**, Illustration of experimental procedures. *FLVCR1* was deleted by polyIC injection in *FLVCR1*$^{f/f}$-Mx1-

851 Cre (knockout) mice. Liver samples of control (*FLVCR1*$^{+/+}$-Mx1-Cre) and knockout mice were collected

852 at least 4 weeks post-injection for metabolomic analysis. **b,** Levels of choline and choline metabolites

853 from control and knockout mice. **c**, Levels of ethanolamine metabolites from control and knockout

854 mice. Each data point represents one mouse. Data are expressed as mean ± SD. ****P<0.0001,

855 ***P<0.001, **P<0.01, *P<0.05. ns, not significant. *t*-test.

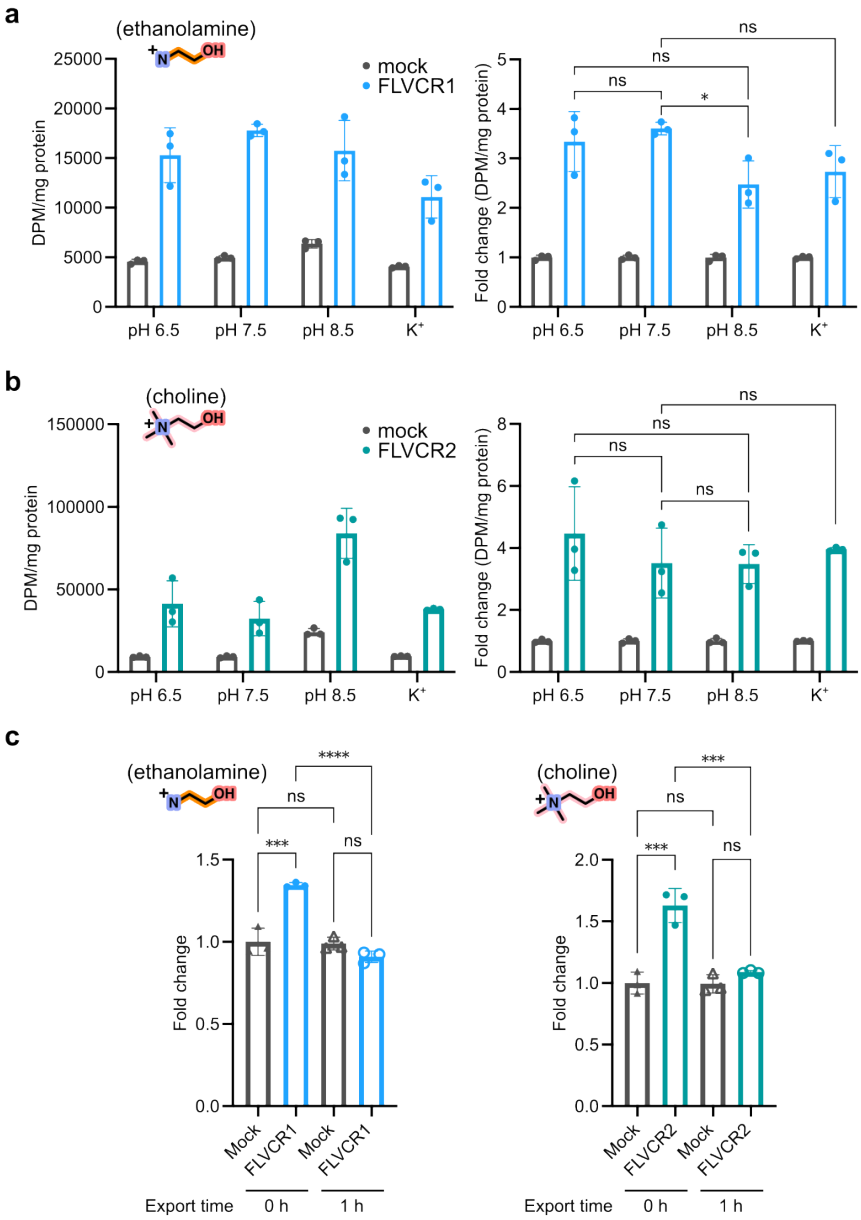

Extended Data Fig. 3: Transport properties of FLVCR1 and FLVCR2.

a, Ethanolamine transport activity of FLVCR1 at indicated pH values, and in sodium-free buffer (K^+). **b,** Choline transport activity of FLVCR2 at indicated pH values, and in sodium-free buffer (K^+). The right panels show normalized data with reference to the respective mocks. In these experiments, 2.5 µM [^{14}C] ethanolamine was used for FLVCR1 or 20 µM [^{3}H] choline for FLVCR2, respectively. The cells were co-expressed with *ETNK-1* or *CHKA* and incubated with the ligands at 37 °C for 15 mins. **c**, Export assays of FLVCR1 with ethanolamine (left) and FLVCR2 with choline (right). In these assays, 100 µM [^{14}C] ethanolamine or 200 µM [^{3}H] choline was incubated with *FLVCR1* or *FLVCR2* overexpression cells, respectively. After 2 hours of incubation, the buffer was washed out. Intracellular [^{3}H] choline or [^{14}C]

866 ethanolamine from the cells was allowed to release into choline/ethanolamine-free medium for 1 hour.
867 The radioactive signal in the cells was normalized to the total protein and expressed as fold change to
868 mock. Each symbol represents one replicate. Data are expressed as mean ± SD. ****P<0.0001,
869 ***P<0.001, *P<0.05. ns, not significant. Two-way ANOVA for (**a**) and (**b**), One-way ANOVA for (**c**).
870

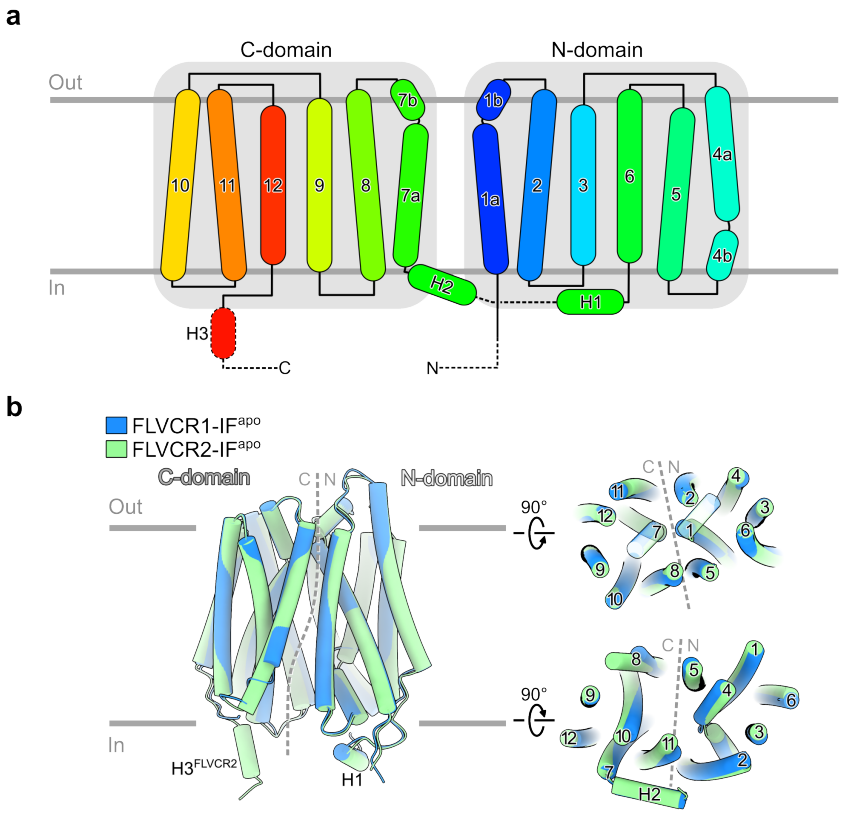

871

872 **Extended Data Fig. 4: Architecture and structural comparison between FLVCR1 and FLVCR2.**

873 **a**, Schematic diagram of FLVCR family showing the topology of the secondary structure. Motifs that

874 are not observed in both cryo-EM structures of FLVCR1 and FLVCR2 are shown as dashed lines. **b**,

875 Structural comparison of FLVCR1-IF^{apo} and FLVCR2-IF^{apo} in tube representation, viewed from the lipid

876 bilayer (left), extracellular side (top-right), and intracellular side (bottom-right).

877

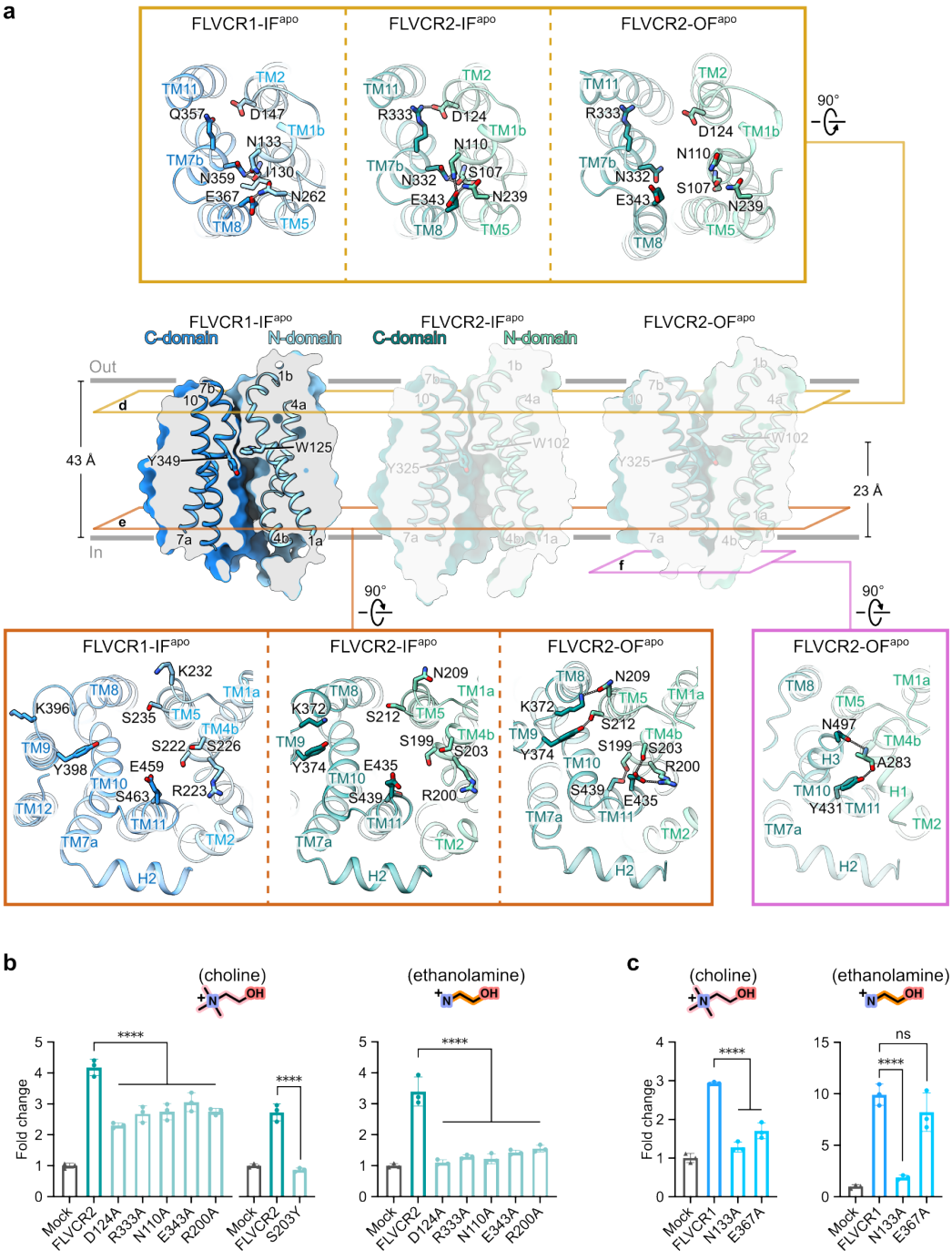

878

879 **Extended Data Fig. 5: Residues for intra- and extracellular gating in FLVCR1 and FLVCR2.**

880 **a**, Cut-away view of FLVCR1-IF^{apo} in surface representation showing the cytoplasmic cavity. Two central
881 aromatic residues are shown as sticks. The structures of FLVCR2-IF^{apo} and FLVCR2-OF^{apo} are shown for
882 comparison. Cross-sections of their inter-domain interactions are shown from the extracellular side
883 (top), or from the intracellular side (bottom-left). Residues in FLVCR1 corresponding to the inter-
884 domain interaction residues in FLVCR2 are shown. The bottom-right panel shows the inter-domain
885 interactions between H1 and H3 in FLVCR2-OF^{apo} viewed from the intracellular side. Residues

886 participating in the inter-domain interactions are shown as sticks; hydrogen bonds and salt bridges are
887 labelled with dashed lines. **b**, Transport assay of FLVCR2 mutants for choline (left) and ethanolamine
888 (right). *CHKA* or *ETNK-1* was co-expressed with wild-type *FLVCR2* and mutant plasmids. In these assays,
889 100 µM [^{3}H] choline or 2.5 µM [^{14}C] ethanolamine was used, respectively. **c**, Transport assay of FLVCR1
890 mutants for choline (left) and ethanolamine (right). *CHKA* or *ETNK-1* was co-expressed with wild-type
891 *FLVCR1* and mutant plasmids, and 20 µM [^{3}H] choline or 2.5 µM [^{14}C] ethanolamine was used,
892 respectively. Each symbol represents one replicate. Data shown are mean ± SD. ****P<0.0001. ns, not
893 significant. One-way ANOVA.
894

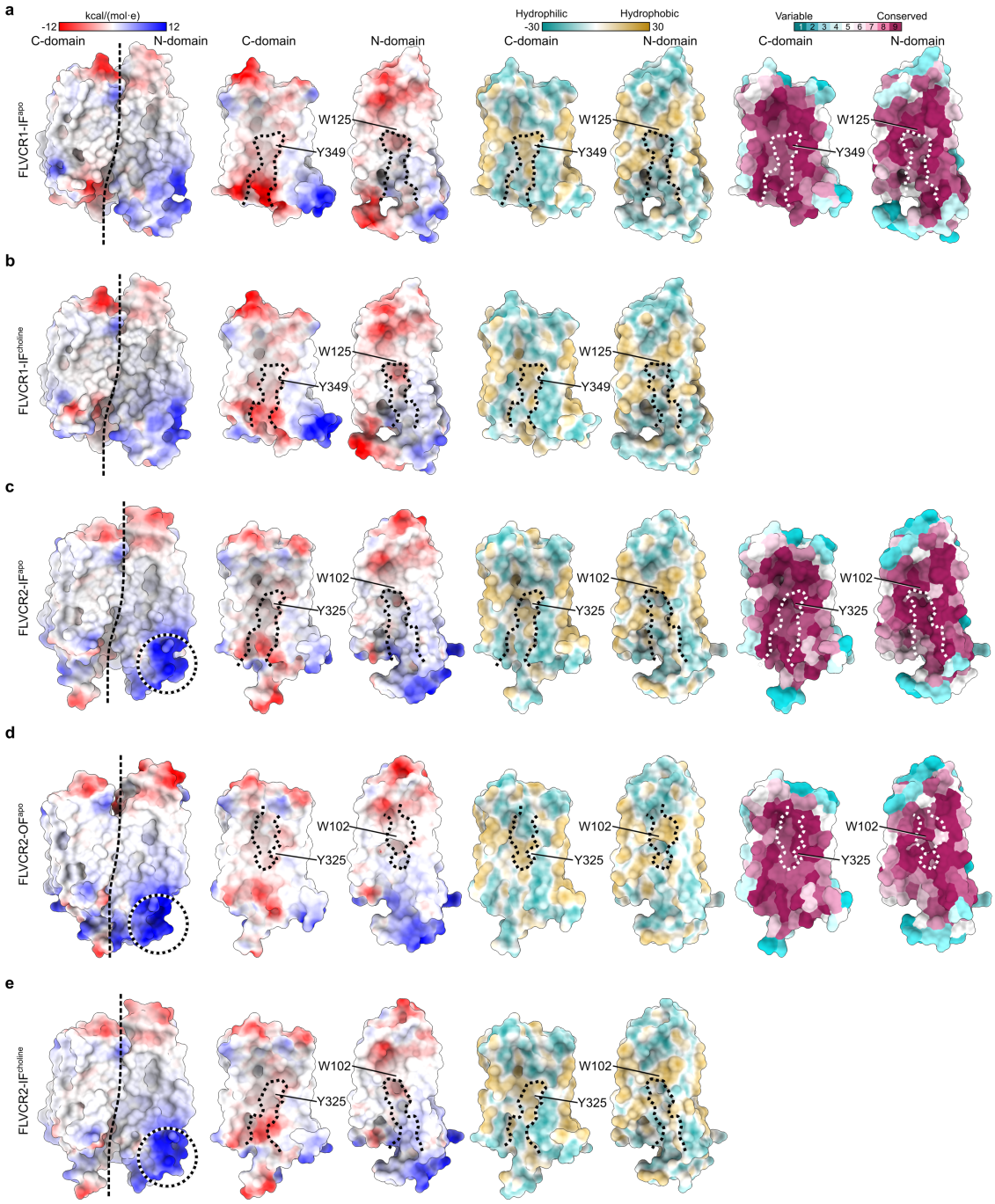

Extended Data Fig. 6: Physicochemical properties of FLVCR structures and conservation analyses. Surface charge, hydrophobicity, and conservation analyses of FLVCR1-IF^{apo} (**a**), FLVCR1-IF^{choline} (**b**), FLVCR2-IF^{apo} (**c**), FLVCR2-OF^{apo} (**d**), and FLVCR2-IF^{choline} (**e**). From left to right: Surface viewed from the lipid bilayer and both C and N domains viewed from the domain interface coloured by electrostatic potential, the domain interface coloured by hydrophobicity, and the domain interface coloured by sequence conservation. The cavity in the different states of both FLVCRs is outlined with dashed lines.

902 Two important central pocket residues (W125 and Y349 in FLVCR1; W102 and Y325 in FLVCR2) are

903 indicated. The FLVCR2 binding site for heme is marked by black-and-white circles.

904

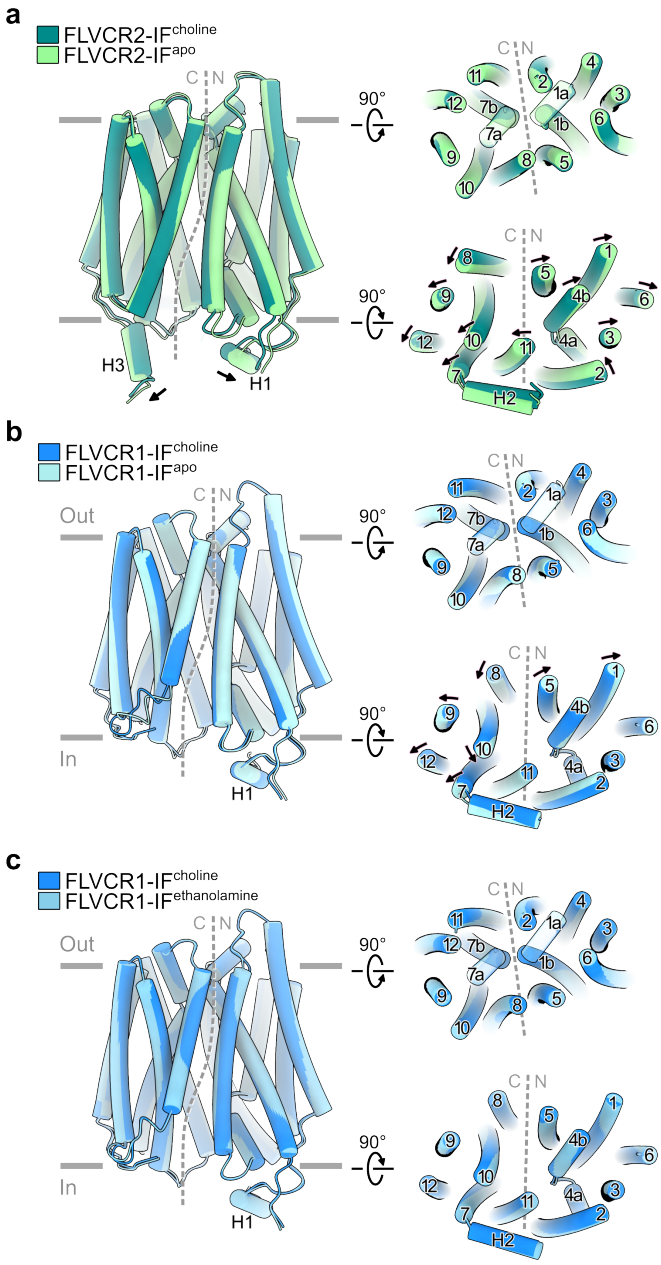

Extended Data Fig. 7: Conformational changes of substrate-bound FLVCRs.

Structural comparison of FLVCR2-IF^{choline} and FLVCR2-IF^{apo} (**a**), FLVCR1-IF^{choline} and FLVCR1-IF^{apo} (**b**), as well as FLVCR1-IF^{choline} and FLVCR1-IF^{ethanolamine} (**c**), viewed from the lipid bilayer (left), extracellular side (top-right), and intracellular side (bottom-right).

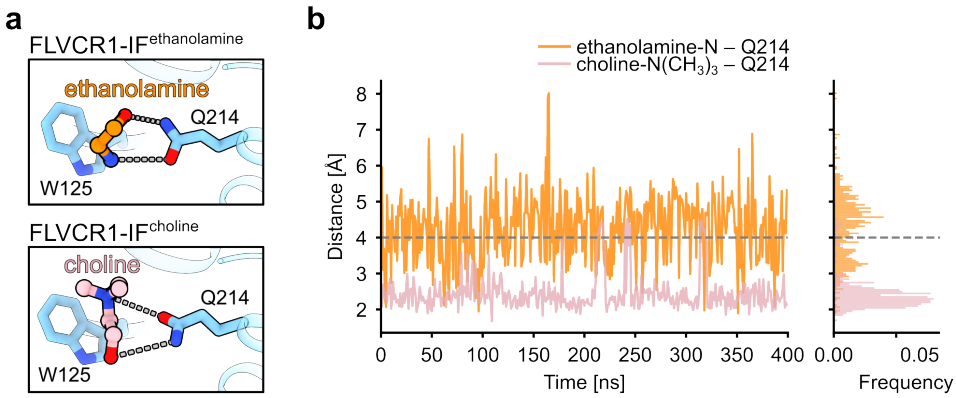

Extended Data Fig. 8: Interaction chemistries and dynamics between Q214F^{LVCR1} and respective ligands..

a, Structural comparison of the binding site of ethanolamine- and choline-bound FLVCR1. **b**, Time-resolved distance plots between Q214 and the primary amine of ethanolamine (orange) or the tertiary amine of choline (pink) obtained from MD simulation runs. The right panel shows the accumulative frequency of their distances during the simulations.

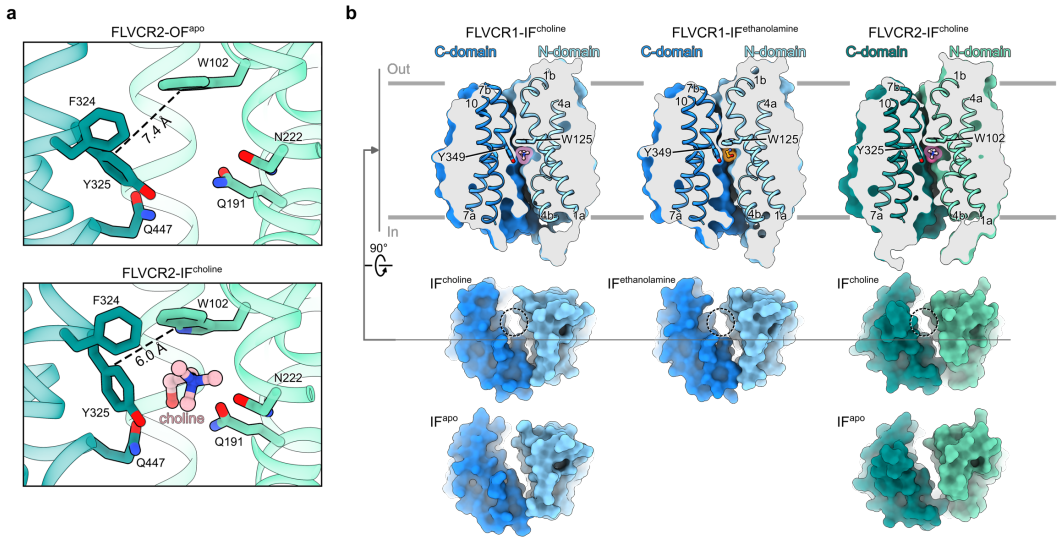

919

920 **Extended Data Fig. 9: Translocation pathway of choline in FLVCRs.**

921 **a**, Choline-binding sites of FLVCR2-OF^{apo} (top) and FLVCR2-IF^{choline} (bottom) with the distance between

922 W102 and Y325 shown as dashed lines. **b**, Cut-away views of FLVCR1-IF^{choline} (top-left), FLVCR1-

923 IF^{ethanolamine} (top-middle) and FLVCR2-IF^{choline} (top-right) showing the inward-facing cavity. Two central

924 aromatic residues are shown as sticks. The surfaces shown below are the respective models viewed

925 from the intracellular side. The surfaces of IF^{apo} of FLVCR1 and FLVCR2 are also shown for comparison.

926 The dashed circles indicate the peripheral channel in the ligand-bound state.

927

928